The Astrophysical Journal, 907:19 (21pp), 2021 January 20 https://doi.org/10.3847/1538-4357/abccc0

The Rise and Emergence of Untwisted Toroidal Flux Ropes on the Sun

K. J. Knizhnik[1], J. E. Leake[2], M. G. Linton[1], and S. Dacie[3]
[1] Naval Research Laboratory, 4555 Overlook Avenue SW, Washington, DC 20375, USA
[2] Heliophysics Science Division, NASA Goddard Space Flight Center, 8800 Greenbelt Road, Greenbelt MD 20771, USA
[3] Max Planck Institute for Meteorology, Bundesstraße 53, D-20146 Hamburg, Germany
Received 2020 July 20; revised 2020 November 20; accepted 2020 November 21; published 2021 January 21

Abstract

Magnetic flux ropes (MFRs) rising buoyantly through the Sun's convection zone are thought to be subject to viscous forces preventing them from rising coherently. Numerous studies have suggested that MFRs require a minimum twist in order to remain coherent during their rise. Furthermore, even MFRs that get to the photosphere may be unable to successfully emerge into the corona unless they are at least moderately twisted, since the magnetic pressure gradient needs to overcome the weight of the photospheric plasma. To date, however, no lower limit has been placed on the critical minimum twist required for an MFR to rise coherently through the convection zone or emerge through the photosphere. In this paper, we simulate an untwisted toroidal MFR that is able to rise from the convection zone and emerge through the photosphere as an active region that resembles those observed on the Sun. We show that untwisted MFRs can remain coherent during their rise and then pile up near the photosphere, triggering undular instability, allowing the MFR to emerge through the photosphere. We propose that the toroidal geometry of our MFR is critical for its coherent rise. Upon emergence, a pair of lobes rises into the corona. The two lobes then interact and reconnect, resulting in a localized high speed jet. The resulting photospheric magnetogram displays the characteristic salt-and-pepper structure often seen in observations. Our major result is that MFRs need not be twisted to rise coherently through the convection zone and emerge through the photosphere.

Unified Astronomy Thesaurus concepts: Solar magnetic fields (1503); Solar magnetic flux emergence (2000); Solar active regions (1974); Solar physics (1476)

1. Introduction

An important unsolved problem in solar physics is the origin of active regions on the photosphere and in the overlying corona. While it is generally agreed that photospheric flux distributions are due to the emergence of sub-photospheric magnetic fields (Parker 1955; see also review by Cheung & Isobe 2014) that are generated by a dynamo process (Parker 1955; Moffatt 1978; Nelson & Miesch 2014), the exact manner in which the magnetic fields make their way from deep in the solar interior to the solar surface is a matter of debate.

First, magnetic flux ropes (MFRs) need to be able to rise through the convection zone. One method that has been studied extensively in the literature is that of a buoyant rise of MFRs (Parker 1955). In these models, a flux rope in the convection zone that is in pressure balance with the outside ambient plasma is either in gravitational or thermal equilibrium with its surroundings. Since the magnetic pressure of the flux rope lowers its internal plasma pressure, if the flux rope is in thermal equilibrium, the density inside the flux rope will be lower than the density outside the flux rope, while the temperature inside and outside will be the same. Conversely, if the flux rope is in gravitational equilibrium, the temperature inside the flux rope will be lower than the temperature outside the flux rope, while the density inside and outside will be the same. In this case, and in the absence of convection, the flux rope can remain stable in the convection zone until thermal conduction brings it into thermal equilibrium, causing the density inside the flux rope to decrease (assuming it maintains pressure balance), making the flux rope buoyant and causing it to rise. Thus, the fate of a pressure balanced flux rope is to be buoyantly unstable as a result of the density deficit caused by the added magnetic pressure. In this picture, therefore, the rise of MFRs through the convection zone is a buoyantly driven process. This model has been used in numerous studies of flux emergence (D'Silva & Choudhuri 1993; Fan et al. 1993; Moreno-Insertis et al. 1994; Schussler et al. 1994; Galsgaard et al. 2007; Archontis et al. 2013; Knizhnik et al. 2018).

One issue with this model is that it has been thought that buoyantly rising flux ropes require a critical twist in order to maintain their integrity against viscosity-generated vortical flows that fragment the flux ropes during their rise (Parker 1979; Schuessler 1979; Longcope et al. 1996; Moreno-Insertis & Emonet 1996; Emonet & Moreno-Insertis 1998; Fan et al. 1998; Wissink et al. 2000; Toriumi & Yokoyama 2011). While Rempel & Cheung (2014) showed that convection supports the integrity of even an untwisted flux rope against these forces so that it can rise coherently through the upper portion of the convection zone, in the absence of convection the twist that is required to withstand viscous fragmentation is unclear. Furthermore, if the flux tube breaks up into fragments, for flux tube vortices with circulation Γ rising with velocity v, the Kutta–Zhukhovsky theorem (Landau & Lifshitz 1987; Batchelor 2000) predicts a force per unit length

$$f = -\rho v \Gamma, \tag{1}$$

which acts perpendicular to the velocity to separate the fragments. The additional horizontal component of the velocity creates its own Kutta–Zhukhovsky force, this time directed downward, eventually bringing the rise to a complete stop. Thus, it seems critical that, for a coherent rise, a flux rope must maintain its integrity against viscous fragmentation, and therefore weakly twisted flux ropes should not be able to rise to the photosphere. In two dimensions, Emonet & Moreno-Insertis (1998) found that the

critical twist necessary for the flux tube to maintain its coherence during its rise depended on a magnetic Weber number

$$\mathrm{We}_m = \frac{E_{\mathrm{kin,rise}}}{E_{\mathrm{mag,twist}}} = \frac{\rho v^2/2}{B_{\mathrm{tw}}^2/8\pi}, \quad (2)$$

where ρ is the density, v is the tube's rise velocity, and B_{tw} is the strength of the twist component of the flux tube's magnetic field. They found that the tube remained coherent if $\mathrm{We}_m < 1$, meaning that a significant twist was needed for a coherent rise. However, three-dimensional studies have shown that the degree of curvature of the rising Ω-loop can significantly reduce the strength of the critical twist field necessary for coherence (Abbett et al. 2000). To this end, MacTaggart & Hood (2009) performed simulations of the emergence of weakly twisted toroidal flux ropes—with $qR = 0.2$, where R is the radius and q is the twist wavenumber—that start out in the shape of a torus. They found that such flux ropes were able to coherently rise and emerge through the photosphere into the corona. However, the twist used by MacTaggart & Hood (2009), though small, leaves open the question of whether MFRs with even smaller twists would be able to rise coherently.

There is a further problem for flux ropes that, having survived the rise through the convection zone, make it to the photosphere. It has been shown that a significant twist is needed in order to emerge through the photosphere without the aid of convection, since the emergence process is thought to occur through a magnetic buoyancy instability (MBI) (Parker 1955; Newcomb 1961; Thomas & Nye 1975; Acheson 1979; Murray et al. 2006; Toriumi & Yokoyama 2010; Archontis et al. 2013; Leake et al. 2013). In this picture, the photosphere forms an interface separating low- and high-density plasma that is modified by the pile-up of flux just below the photosphere. Perturbations that bend the field lines can easily grow, since plasma drains from the concave-down field lines, unburdening them and allowing them to rise further (Fan 2001).

Murray et al. (2006) found that flux ropes needed to be at least moderately twisted to be able to exceed the threshold for this instability, and that weakly twisted flux ropes were unable to emerge through the photosphere. At low twists, at values of about $qR = 0.25$, they found that the gradient of the magnetic field was too small near the photosphere to overcome the weight of the plasma. Similarly, Toriumi & Yokoyama (2011) performed a simulation of the rise of weakly twisted cylindrical flux ropes from deep in the solar interior. They found that at twists below $qR = 0.25$, the flux ropes failed to emerge through the photosphere, but that at higher twists, the MBI was triggered and flux ropes were able to emerge.

Subsequently, Archontis et al. (2013) ran a simulation of a weakly twisted flux rope with the same twist ($qR = 0.25$) as that used by Murray et al. (2006) and Toriumi & Yokoyama (2011) and found that it did, in fact, emerge through the photosphere if given enough time, and attributed the emergence to the MBI. They found that the emergence occurred quite differently than a typical moderately twisted flux rope. Instead of forming a simple arcade in the corona, such as that formed in the emergence of the toroidal flux rope of MacTaggart & Hood (2009), the weakly twisted flux rope formed two distinct arcades that they termed "magnetic lobes," separated by a neutral line. The MBI allowed portions of the flux rope to emerge into the corona, while keeping other parts of the flux rope submerged. The concave-down portions of the field were able to emerge, whereas the concave up portions containing heavy plasma remained stuck below the photosphere. Additional plasma draining down from the emerging loops onto the submerged loops exacerbated the situation. Further, they found that the two lobes interacted and reconnected, causing a high speed jet and a reconfiguration of the field.

The contrasting results of Murray et al. (2006), Toriumi & Yokoyama (2011) and Archontis et al. (2013) for the same twist raises the question of whether there is, in fact, a critical twist that determines whether flux ropes will emerge or not, or whether there are additional considerations in whether emergence occurs. Toriumi & Yokoyama (2011) and Archontis et al. (2013) used different field strengths and depth-to-radius ratios: Toriumi & Yokoyama (2011) used a field strength of 15 kG and a depth-to-radius ratio of 20, whereas Archontis et al. (2013) used a field strength of 2.8 kG and depth-to-radius ratio of <5. In addition, the flux rope of Toriumi & Yokoyama (2011) was initially placed about 10 times deeper than the flux rope of Archontis et al. (2013). As a result, a direct comparison is difficult to perform and there are indications that the flux ropes of Toriumi & Yokoyama (2011) did, in fact, emerge, or would have had the simulation been run for longer (see, for example, Figure 10 of Toriumi & Yokoyama 2011). As a result, the question of just how weakly twisted a flux rope can be before emergence is suppressed remains open.

The picture that *emerges,* therefore, is one in which a critical twist is posited to be necessary for MFRs to rise coherently through the convection zone, and a (perhaps different) critical twist is thought to be required for MFRs to emerge through the photosphere. While some numerical studies, described above, have constrained the value of these twists, no lower limit has yet been set. Furthermore, the critical twist cannot be constrained observationally, since there is an apparent discrepancy between observed twists and theoretically estimated values. Several authors have measured the twist in active regions to be of order $0.01\,\mathrm{Mm}^{-1}$ (Pevtsov et al. 1994, 1995, 1997; Longcope et al. 1998, 1999). On the other hand, Toriumi & Yokoyama (2011) struggled to emerge flux ropes with twists as "low" as $0.25/R$. For their flux rope of radius 0.43 Mm, this converts to a twist of $0.59\,\mathrm{Mm}^{-1}$, which is more than an order of magnitude higher than observed. Thus, there is already a huge gap between the observed twists and flux ropes that were too weakly twisted to emerge. This discrepancy between observations and theory has been discussed previously in Knizhnik et al. (2018). They argued that the "twist" as measured in the photosphere of their simulations has little physical correspondence to the twist as measured by the rotation of field lines per unit length in the subsurface flux rope. Since there is expected to be significant reconnection, diffusion, and possibly kinking of the flux rope as it rises, the twist at the photosphere would consequently be reduced. In addition, significant twist may remain trapped below the photosphere (Fan 2009). Thus, twists measured at the photosphere are unlikely to constrain the subsurface twist of rising flux ropes.

In this study, we perform a simulation of a completely untwisted toroidal flux rope rising from inside the convection zone, and show that it is able to emerge, implying that in the absence of twist, strong axial curvature is a necessary property for MFRs to both rise coherently through the convection zone or emerge through the photosphere. This paper is organized as follows. In Section 2, we describe our numerical model. In Section 3, we show the results of the rise and emergence of an

untwisted toroidal flux rope. In Section 4, we summarize our results and compare them to the previous studies.

2. Numerical Model

2.1. MHD Equations

Our numerical model uses the visco-resistive MHD Lagrangian-remap code Lare3D (Arber et al. 2001). It solves the equations of MHD having the Lagrangian form of

$$\frac{D\rho}{Dt} = -\rho\nabla\cdot\boldsymbol{v}, \tag{3}$$

$$\frac{D\boldsymbol{v}}{Dt} = -\frac{1}{\rho}(\mu_0^{-1}(\nabla\times\boldsymbol{B})\times\boldsymbol{B} + \nabla P + \rho\boldsymbol{g} + \nabla\cdot S_{ij}), \tag{4}$$

$$\frac{De}{Dt} = \frac{1}{\rho}\left(-P\nabla\cdot\boldsymbol{v} + \Xi_{ij}S_{ij} + \frac{\eta}{\mu_0^2}(\nabla\times\boldsymbol{B})^2\right), \tag{5}$$

$$\frac{D\boldsymbol{B}}{Dt} = (\boldsymbol{B}\cdot\nabla)\boldsymbol{v} - \boldsymbol{B}(\nabla\cdot\boldsymbol{v}) - \eta\nabla^2\boldsymbol{B}. \tag{6}$$

In these equations, ρ is the mass density, $\boldsymbol{v}$ is the velocity, $\boldsymbol{B}$ is the magnetic field, and e is the specific energy density. μ_0 is the permeability of free space, which is used to relate the magnetic field to the current density $\mu_0\boldsymbol{J} = \nabla\times\boldsymbol{B}$. $\eta = 16\,\Omega\,\mathrm{m}$ is the resistivity, $\boldsymbol{g} = -274\ \mathrm{ms}^{-2}\hat{\boldsymbol{z}}$ is the gravity at the photosphere, and $\boldsymbol{S}$ is the stress tensor with components given by

$$S_{ij} = \nu\left(\Xi_{ij} - \frac{1}{3}\delta_{ij}\nabla\cdot\boldsymbol{v}\right). \tag{7}$$

The viscosity $\nu = 3.35\times10^3\,\mathrm{kg\,m^{-1}\,s^{-1}}$, δ_{ij} is the Kronecker delta function, and Ξ can be written in terms of the components of the Jacobian matrix $\nabla\boldsymbol{v}$ as

$$\Xi_{ij} = \frac{1}{2}\left(\frac{\partial v_i}{\partial x_j} + \frac{\partial v_j}{\partial x_i}\right). \tag{8}$$

The gas pressure is defined through the mass density, Boltzmann constant k_B, temperature T and reduced particle mass μ_m as

$$p = \frac{k_B\rho T}{\mu_m}, \tag{9}$$

where $\mu_m = 1.25m_p$, with m_p the proton mass. This choice of mass is discussed in Leake et al. (2013) and Leake & Linton (2013). The pressure is related to the specific energy density via

$$e = \frac{p}{\rho(\gamma-1)}, \tag{10}$$

where $\gamma = 5/3$ is the ratio of specific heats. Lare3D defines the plasma variables e and ρ on the cell centers, magnetic field components at cell faces, and the velocity components at the cell vertices, and preserves $\nabla\cdot\boldsymbol{B}$.

2.2. Normalization

The MHD equations are scaled by choosing three quantities to normalize the physical parameters. We choose a normalizing field strength

$$B_0 = 0.13T, \tag{11}$$

length scale

$$L_0 = 1.7\times10^5\,\mathrm{m}, \tag{12}$$

(which is the photospheric pressure scale height), and gravitational acceleration

$$g_0 = g_{\mathrm{sun}} = 274\ \mathrm{m\,s^{-2}}. \tag{13}$$

These choices constrain the normalizing values for the gas pressure

$$P_0 = \frac{B_0^2}{\mu_0} = 1.3\times10^4\,\mathrm{Pa}, \tag{14}$$

mass density

$$\rho_0 = \frac{B_0^2}{\mu_0 L_0 g_0} = 3\times10^{-4}\,\mathrm{kg\,m^{-3}}, \tag{15}$$

velocity

$$v_0 = \sqrt{L_0 g_0} = 6.8\times10^3\,\mathrm{m\,s^{-1}}, \tag{16}$$

time

$$t_0 = \sqrt{\frac{L_0}{g_0}} = 24.9\,\mathrm{s}, \tag{17}$$

temperature

$$T_0 = \frac{m_p L_0 g_0}{k_B} = 5.6\times10^3\,\mathrm{K}, \tag{18}$$

current density

$$J_0 = \frac{B_0}{L_0\mu_0} = 0.6\,\mathrm{A\,m^{-2}}, \tag{19}$$

viscosity

$$\nu_0 = P_0 t_0 = 3.35\times10^5\,\mathrm{kg\,m^{-1}\,s^{-1}}, \tag{20}$$

and resistivity

$$\eta_0 = \mu_0 v_0 L_0 = 1.6\times10^3\,\Omega\,\mathrm{m}. \tag{21}$$

2.3. Domain and Boundary Conditions

The simulation domain has the extents $X\times Y\times Z = [-492, 492]L_0\times[-492, 492]L_0\times[-220, 598]L_0$. In the x- and y-directions, we use 1024 grid points, for a resolution of $\delta x = \delta y \approx L_0$, while in the z-direction, 400 grid points are used, but the grid is stretched so that the grid spacing has the form

$$\delta z = L_0\frac{1 + f_0\left[1 + \tanh\left(\frac{z-L_v}{w}\right)\right]}{1 + f_1\left[\tanh\left(\frac{z+f_2}{f_3}\right) - \tanh\left(\frac{z+f_4}{f_5}\right)\right]}. \tag{22}$$

Here, $f_0 = 4.0$, $f_1 = 2.0$, $f_2 = -2.0L_0$, $f_3 = 5.0L_0$, $f_4 = -117.0L_0$, $f_5 = 5.0L_0$, $L_v = 100L_0$, and $w = L_z/20$. Figure 1 shows a profile of δz, along with the local scale height and number of grid points per local scale height. Near the photosphere, $\delta z = 0.25L_0$, so that a minimum of four grid points resolve the photospheric pressure scale height, while farther away from the photosphere, the resolution coarsens, though the number of grid points per scale height increases.

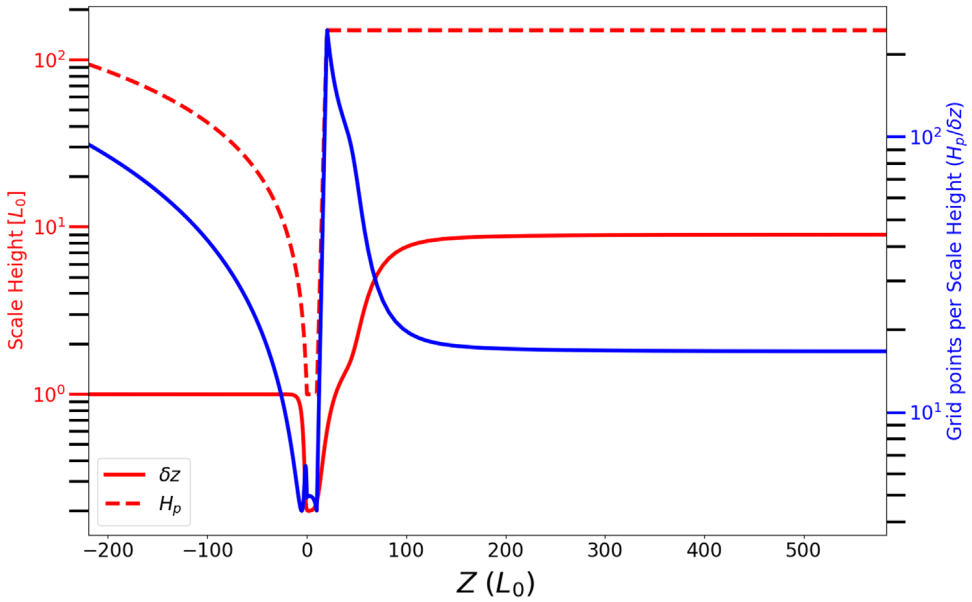

Figure 1. Profiles with height of grid spacing δz (red solid line), pressure scale height (red dashed line), and grid points per local scale height (blue line).

At the boundaries, all velocity components and normal gradients of the magnetic field, plasma density and specific energy density are set to zero. As in Leake et al. (2013), the resistivity is smoothly decreased to zero close to the bottom boundary to reduce diffusion of the magnetic field. In addition, a damping region is applied to the velocity at all four side boundaries, as described in Leake et al. (2013). This prevents reflected waves from interacting with the solution in the interior. As a result of these boundary conditions, the field lines are line-tied at the bottom boundary ($v_h = 0$ and $\eta = 0$).

2.4. Initial Conditions

The simulations are initialized with a hydrostatic background atmosphere with a convection zone ($-220L_0 < z < 0$), a photosphere/chromosphere ($0 < z < 10L_0$), transition region ($10L_0 < z < 20L_0$), and corona ($z > 20L_0$).

In the convection zone, the atmosphere is polytropic, with the temperature following

$$T_{cz}(z) = T_0\left(1 - \frac{z}{l_c}\right), \tag{23}$$

where $l_c = (g\mu_m/k_B)(\gamma - 1)/\gamma$. In the photosphere, $T(z) = T_0$, $\rho(z) = \rho_0$ and $P(z) = P_0$. In the corona, the temperature is

$$T_{\rm cor}(z) = 150T_0. \tag{24}$$

The photosphere and corona are connected by the transition region, where the temperature increases from $T_{\rm ph}$ to $T_{\rm cor}$ via

$$T_{\rm tr}(z) = T_0\left(\frac{T_{\rm cor}}{T_0}\right)^{(z-10L_0)/10L_0} \tag{25}$$

We then numerically integrate $\nabla P = -\rho g$ and the ideal gas law, Equation (9), to obtain the density and pressure profiles throughout the atmosphere.

We place a toroidal flux rope in the convection zone. In spherical coordinates (r, θ, ϕ), the flux rope has the form

$$\boldsymbol{B} = \nabla \times (A(r, \theta)\hat{\phi}) + B_\phi(r, \theta)\hat{\phi}, \tag{26}$$

where

$$B_\phi(r, \theta) = \frac{aB_t}{r\sin\theta}\exp(-\varpi^2/a^2), \tag{27}$$

and

$$A(r, \theta) = \frac{1}{2}\zeta ar\sin\theta B_\phi(r, \theta), \tag{28}$$

and

$$\varpi^2 = r^2 + r_0^2 - 2rr_0\sin\theta. \tag{29}$$

Note that a more general form of this profile is given in Fan (2008). In these equations, $r_0 = 120\,L_0$ and $a = 20\,L_0$ represent the major and minor radii of the flux rope, $B_t = 100\,B_0$ is the initial field strength, and ζ is a dimensionless number representing the flux rope's twist. In terms of the Cartesian coordinates (x, y, z),

$$r^2 = x^2 + (z - z_0)^2, \tag{30}$$

$$\theta = \arccos\left(\frac{x}{r}\right), \tag{31}$$

and

$$\phi = \arctan\left(\frac{z - z_0}{y}\right) \tag{32}$$

are the radial, azimuthal, and toroidal coordinates, respectively, and $z_0 = -220\,L_0$. Thus, our initial flux rope depth-to-radius ratio is similar to that of MacTaggart & Hood (2009), who used $z_0/a = 10.0$ and $z_0/r_0 = 1.7$, compared to our values of 11.0 and 1.8, respectively, though our flux rope is placed about nine times deeper.

We perturb the background plasma and energy densities by

$$\rho(r, z) = \rho_b(z)\left(1 - \frac{p_1(r)}{p_0(z)}\right) \tag{33}$$

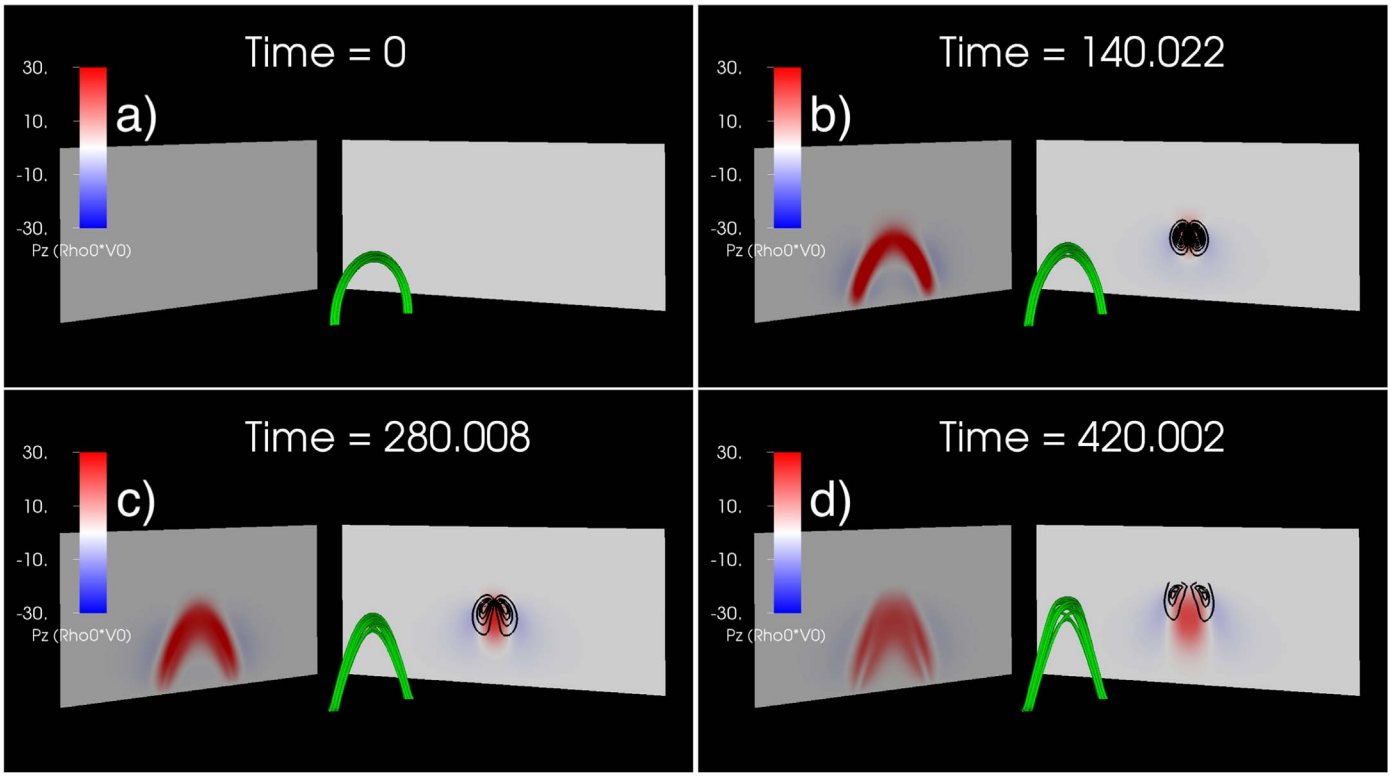

Figure 2. Field lines in the torus at different times during the simulation, traced from the bottom boundary. Color shading shows vertical momentum p_z, and contours show out-of-plane vorticity. The two vertical cuts are taken in the $x = 0$ and $y = 0$ midplanes, respectively, but plotted on the boundaries for clarity. Only the lower part of the domain is shown, from the bottom boundary to about 120 L_0 above the photosphere.

and

$$e(r, z) = \frac{p_0(z) - p_1(r)}{\rho(r, z)(\gamma - 1)}, \tag{34}$$

where p_1 is given by

$$p_1(r) = \frac{1}{2\mu_0} B_\phi^2(r, \theta). \tag{35}$$

In this way, the entire flux rope is made buoyant, but the largest buoyancy is near the center at $x = y = 0$ and $z = z_0 + r_0$.

In the present study, we set $\zeta = 0$, so that the only nonzero component of $\boldsymbol{B}$ is B_ϕ (Equation (27)), corresponding to a completely untwisted flux rope that is bent into the shape of a torus.

3. Results

3.1. Rise through the Convection Zone

Figure 2 shows field lines comprising the torus traced from the fixed bottom boundary at different times during the simulation, where the background color shading shows vertical momentum p_z, and the contours on the $y = 0$ plane represent the out-of-plane (y-directed) vorticity. Both vertical cuts, taken at $x = 0$ and $y = 0$, respectively, are plotted on the side boundaries of the simulation ($x = -492\,L_0$ and $y = -492\,L_0$) for clarity. Only the lower part of the domain is shown, from the bottom boundary to just above the photosphere. The rise of the flux rope manifests itself as a straightening of the legs of the torus, as its bottom end is anchored at the bottom boundary. The semicircular nature of the torus gradually changes to a more diagonally oriented pair of legs. Meanwhile, vortices are generated by the rising flux rope below the photosphere, visible in the $y = 0$ cuts in panels (b–d). These vortices have no observable effect on the evolution of $|B|$ shown in Figures 3 and 4, which show the field strength of the flux rope as a function of time in the y–z and x–z planes. Figure 3 shows that the field strength at the apex of the rising flux rope decreases as it rises, and the semicircle of the torus axis is gradually transformed into more of a triangular shape. Meanwhile, Figure 4 shows that the cross section gradually deforms from the circular shape to a more elongated, oval-like shape, before spreading out as the flux rope approaches the surface. Although the field weakens with time (note the changing color table), there is no hint of fragmenting of the flux rope, and no evidence of vortical magnetic structures breaking off the rope, as is often seen in weakly twisted 2D flux ropes (Schuessler 1979; Longcope et al. 1996). Evidently, this flux rope is able to maintain its coherence throughout its rise, despite the generation of velocity vortices, implying that the curvature of the axis plays an important role in maintaining the integrity of the flux rope (Abbett et al. 2000).

3.2. Photospheric Evolution

Figure 5 shows the photospheric magnetic field distribution at several times during the simulation. Around $t = 776$, the flux rope first appears at the photosphere as a pair of triangular shaped opposite polarity regions, enclosed by a circular band of flux. By $t = 812$, these polarities are in the process of fragmenting, and two small perturbations developed between them, resembling a pair of crescents in the photosphere. Around $t = 860$, the entire region is overwhelmed by narrow lanes of adjacent positive and negative flux. The primary

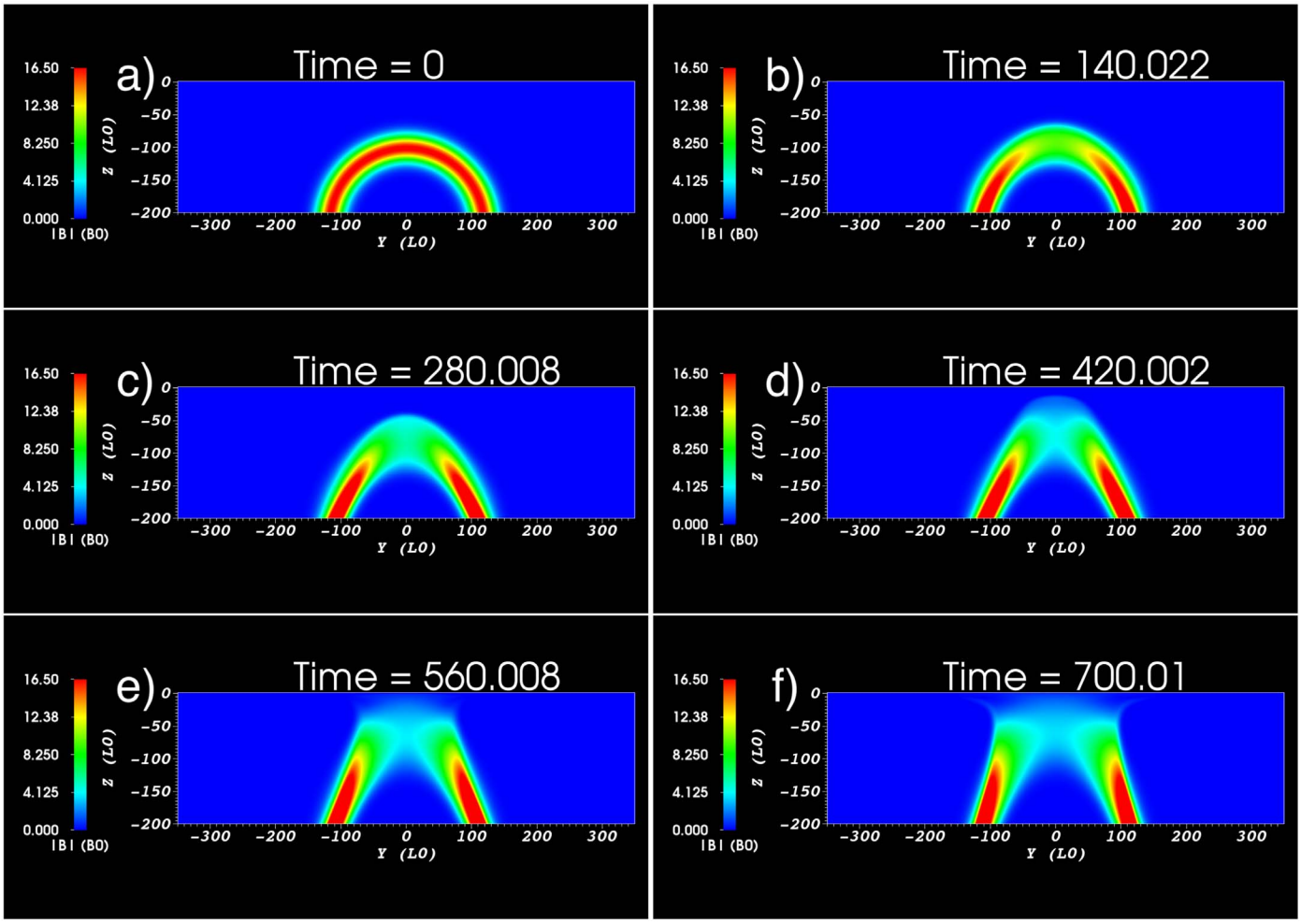

Figure 3. Contours of $|B|$ at different times during the simulation in the y–z plane.

polarities are basically no longer visible at this time. The narrow lanes, in turn, grow significantly, forming many extended lanes on the photosphere. Many of these lanes are oriented at $\pm 45^\circ$ to the x–y axes. The main polarities are now located around $(x, y) = (0, \pm r_0)$, but are difficult to distinguish. In other words, the distance between these two primary polarities is approximately equal to the diameter of the initial toroidal flux rope. The photospheric field shows perturbations growing over the next $\approx 140\, t_0$, with the separation of the two primary polarities merely increasing slightly, but becoming more pronounced. The horizontal magnetic field magnitude $|B_h| = \sqrt{B_x^2 + B_y^2}$, shown in Figure 5(f), shows that the strongest horizontal field is near the central region where the field is mostly trapped just below the surface (see Section 3.3).

3.3. Coronal Evolution

Figures 6 and 7 show field lines in the emerging flux rope as it rises through the convection zone and photosphere. In these figures, field lines are traced from inside each of the legs of the torus on the bottom line-tied boundary. The color of the field line denotes the different behaviors evident in the figure, with the seed points being identical for each panel. In these figures, the left panels are viewed from nearly directly above, while the right panels are viewed close to side-on. When the flux rope initially emerges (panels (a, b) of Figure 6; $t = 776\, t_0$), the red field lines are so curved that they are able to rise just above the photosphere, forming a bipolar active region. Blue and green field lines flatten out sideways as the flux rope approaches the photosphere, and the yellow field lines come up after them. In panels (c, d) ($t = 812\, t_0$), the red field lines have expanded to form lobes in the corona, and the blue and green field lines have still not emerged but have, instead, piled up near the photosphere. The yellow field lines undulate in and out of the photosphere, forming the crescents that are seen in the photospheric field.

In panels (a, b) of Figure 7 ($t = 60\, t_0$), the yellow field lines in the middle of the flux rope undulate, in a serpentine manner, into and out of the photosphere, while the red field lines do the same just above the photosphere. These are highly reminiscent of the sea-serpent topology thought to be responsible for Ellerman bombs (Pariat et al. 2004, 2006; Isobe et al. 2007; Archontis & Hood 2009; Pariat et al. 2009; Danilovic 2017), which are associated with emergence resulting from the undular instability (Isobe et al. 2007). In panels (c, d) ($t = 900\, t_0$), the emergence continues via the formation of a pair of magnetic lobes, evident in the red field lines, which manage to rise higher than the other field lines, possibly due to a series of reconnection events. Reconnection between these lobes, discussed below in Section 3.6, results in the formation of an overlying (pink) field. Note that the side-on view shows that red field lines are really close to the photosphere at

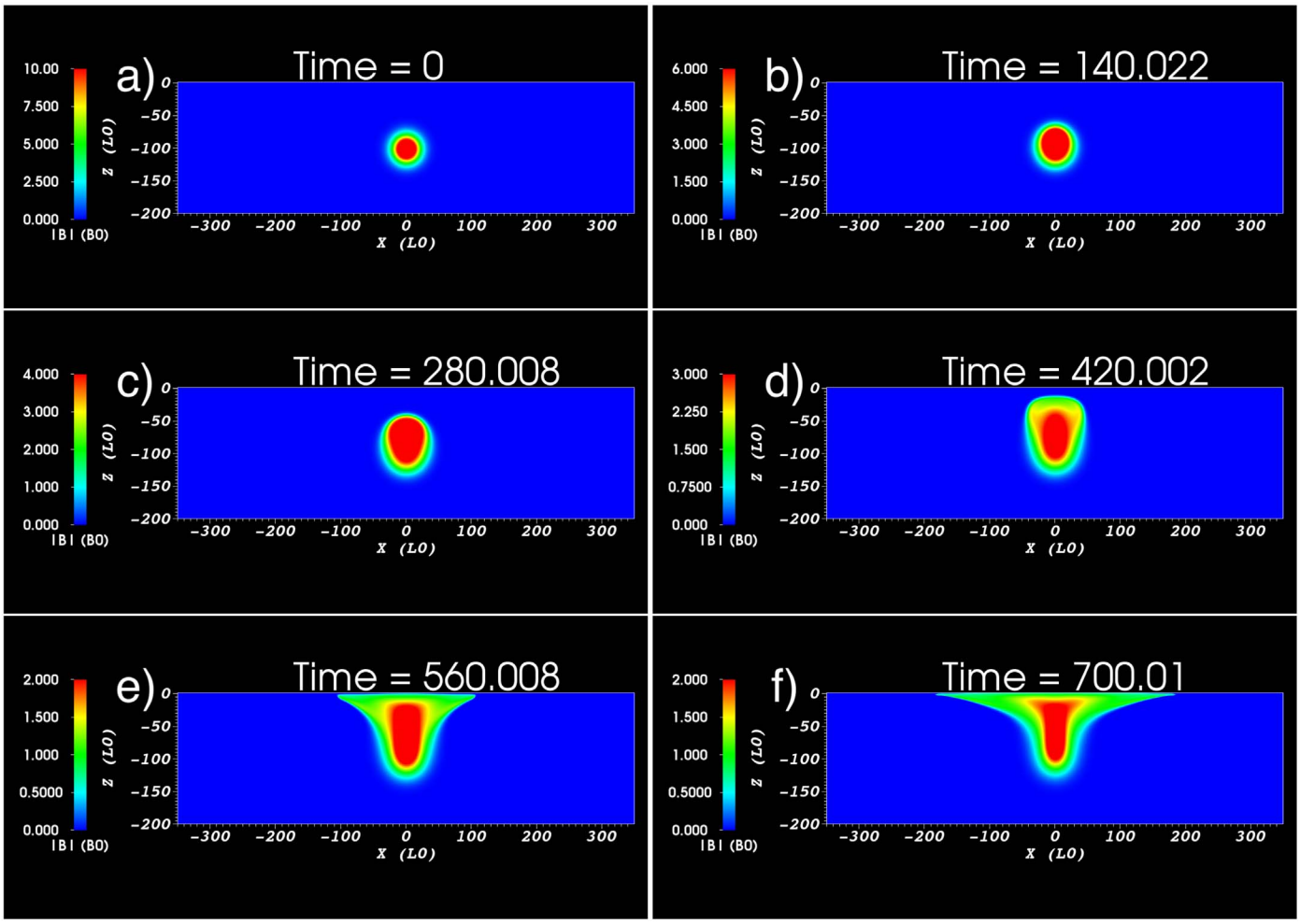

Figure 4. Contours of $|B|$ at different times during the simulation in the x–z plane.

$t = 860\,t_0$ (Figure 7(b)), but reach much higher at $t = 900\,t_0$ (Figure 7(d)). The central portions of these field lines are prevented from rising, as they are supporting heavy photospheric plasma, which is unable to drain. Meanwhile, the blue and green field lines remained flattened sideways.

The evolution of this simulation is markedly different from that shown for the smaller scale, weakly twisted flux rope shown in MacTaggart & Hood (2009), where two well-defined, large polarities form at the photosphere, with very little to no structure in between. At the coronal level, MacTaggart & Hood (2009) found a simple sheared arcade between the two polarities, whereas this simulation displays a series of $\mathcal{M}$-shaped loops connecting the two polarities that correspond to the flux rope's legs. We postulate below that this difference is due to the relative horizontal extent of the simulated emerging regions compared to the 170 km photospheric pressure scale height.

Figure 8 shows the photospheric field and sample field lines at the end of the simulation ($t = 1000\,t_0$). As will be described in Section 3.6, by this point the magnetic lobes seen in panels (c, d) of Figure 7 will have reconnected with each other, causing a reorganization of the magnetic field. Thus, the original field lines plotted above have changed their connectivities. To best represent the coronal field, the field lines shown here are different than the ones shown in Figures 6 and 7. At this stage, some remnants of the pre-interaction behavior can still be observed. The yellow, red, green, and blue field lines are spread outwards, undulating in and out of the photosphere, connecting the two primary polarities. Overlying the entire flux system are a set of pink field lines, which result from reconnection of the magnetic lobes (described below, in Section 3.6).

3.4. Comparison with Observations

An interesting feature of this simulation, as can be seen in Figure 5, is the salt-and-pepper nature of the photospheric magnetogram. It is reminiscent of observational signatures, which are often attributed to the presence of convection breaking up emerging flux bundles (Kitiashvili et al. 2015), which then coalesce back into large-scale polarities (Dacie et al. 2016). Such salt-and-pepper features have been observed in convectively unstable simulations (Rempel & Cheung 2014), but, to date, have not been seen in convectively stable simulations (e.g., Leake et al. 2013), which typically form coherent polarity concentrations. A characteristic quantitative feature of such salt-and-pepper magnetograms is that the flux strength distribution obeys a power law with a slope in the range of $[-1.6, -1.5]$ between 10^1 and 10^3 G early in the active region's life cycle, though slopes as steep as -2.0 and as shallow as -1.3 were also measured (Dacie et al. 2016). In view of these results, Dacie et al. (2017) analyzed multiple simulations of emerging flux ropes and found that the convectively stable simulations from Leake et al. (2013) and MacTaggart & Hood (2009), with buoyant twisted cylindrical

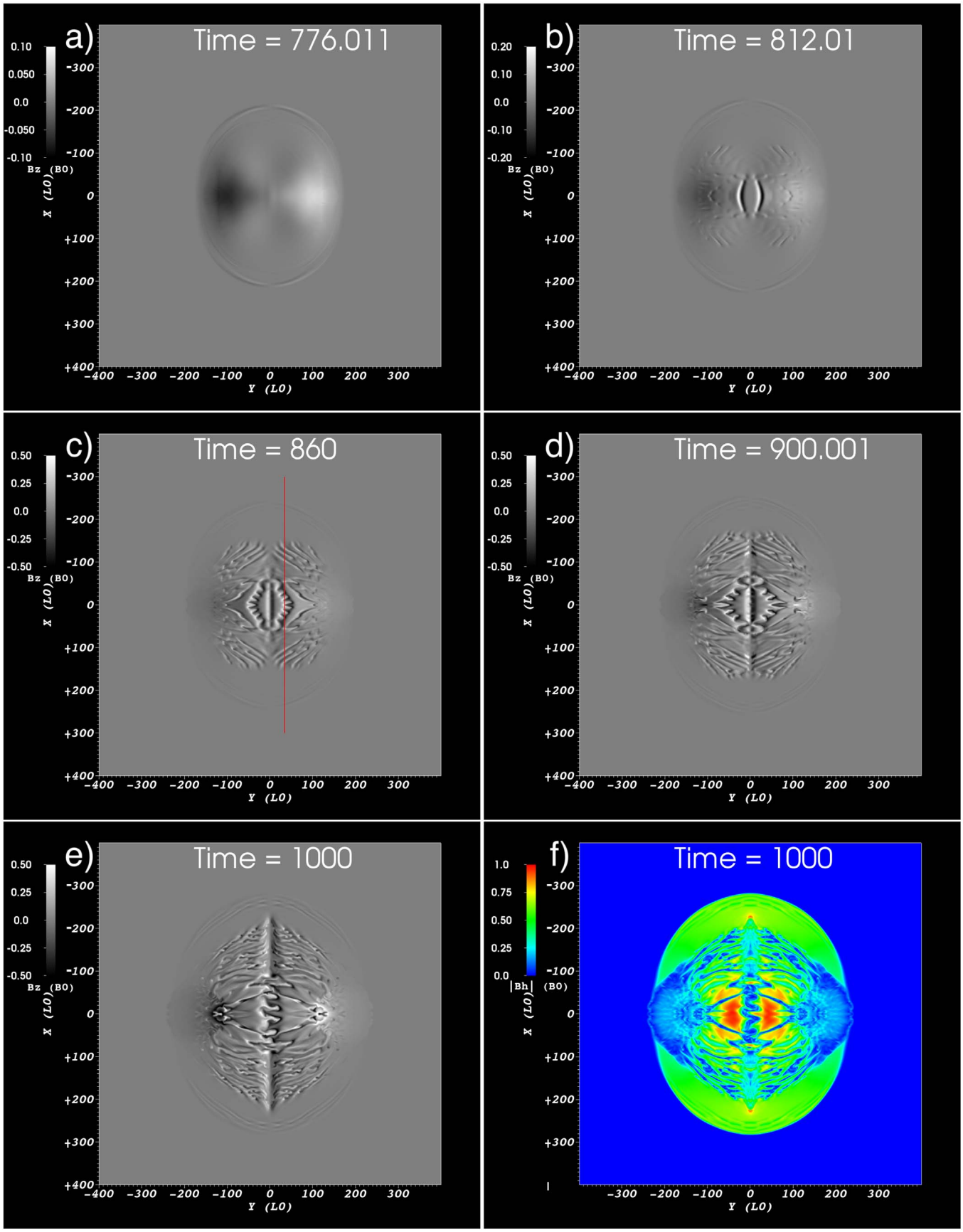

Figure 5. Photospheric B_z at different times throughout the simulation. The red line in panel (c) shows the location of the cut analyzed in Figure 14. The last panel shows the magnitude of the in-plane magnetic field.

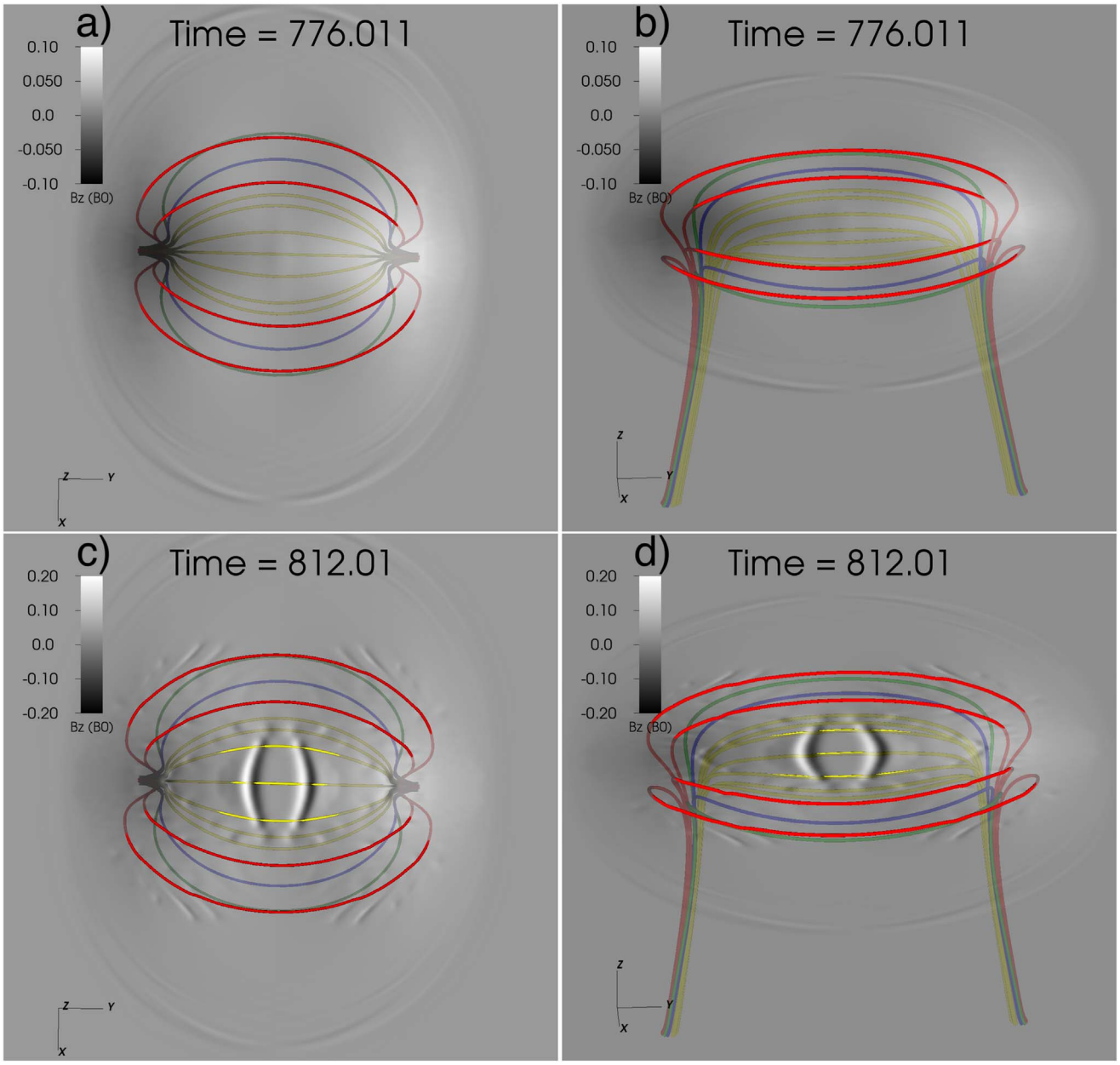

Figure 6. Field lines, overplotted on photospheric magnetograms, at various stages early in the simulation. The seed points for these field lines are the same as in Figure 7.

and toroidal flux ropes, respectively, produced flux distribution slopes in the correct range only during the later phases of emergence. Those simulations did not show the signatures of the undular instability observed here. Meanwhile, the convective simulation of Rempel & Cheung (2014) was able to generate a power law over the range of 10^1–10^3 G in field strength, with slopes in the range of $[-1.4, -1.0]$ over the entire duration of the emergence. Thus, it seems that convective simulations produced the proper range of large and small field strengths, while buoyant twisted flux ropes without convection could produce the proper range of small and large field strengths only during the later phases of emergence, when the primary polarities had become coherent. Since our simulation shows qualitative differences from the coherent emergence of Leake et al. (2013) and MacTaggart & Hood (2009), an interesting question is what is the photospheric flux distribution in our simulation?

We performed a kernel density estimation (Dacie et al. 2016, 2017) on this simulation by converting our magnetic field values to Gauss (see Equation (11)), and we plotted the results in Figures 9 and 10. At each time, we fit a line to the distribution between 20 G and $\frac{2}{3}B_{-3}$, where B_{-3} is defined as the magnetic field strength where the slope of the distribution curve exceeds -3 (vertical red line in Figure 9, i.e., the dashed red line is fit up to $2/3$ of the value at which there is an approximate knee in the distribution). The temporal profile of the slope of this distribution is shown in Figure 10. The gray area denotes the range of slopes observed by Dacie et al. (2017). As can be seen from these figures, the slope of the distribution is relatively steep only during the very early time period, around $t = 800$–$830\,t_0$, corresponding approximately to the linear phase of the undular instability (see Section 3.5). After this early phase, the slope rapidly becomes less steep,

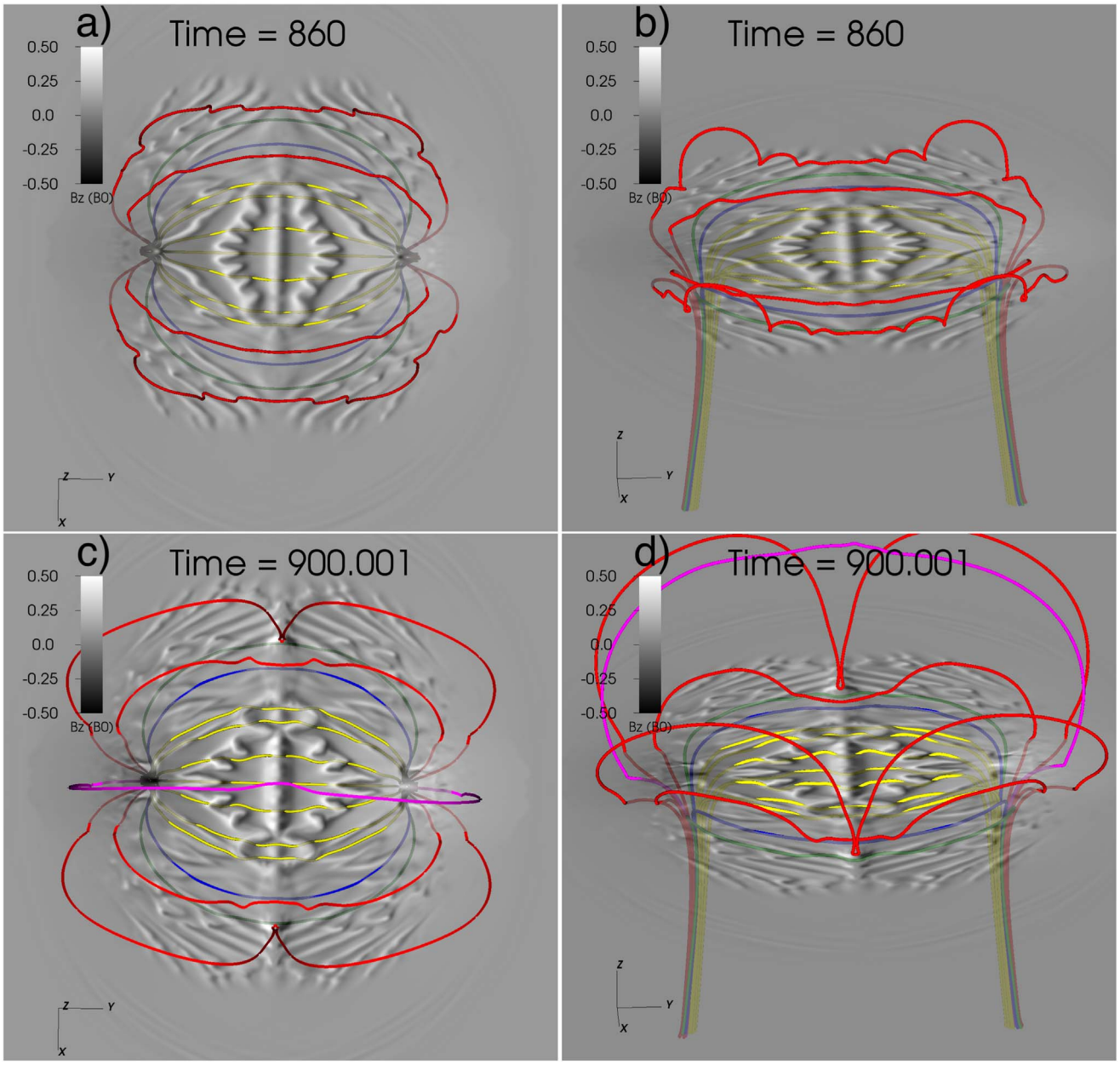

Figure 7. Field lines, overplotted on photospheric magnetograms, at various stages in the middle of the simulation. The seed points for these field lines are the same as in Figure 6.

getting to values of approximately −1 for the rest of the emergence. Thus, we find that even in the absence of convection, small-scale salt-and-pepper structure that resemble observations can be produced during the linear phases of emergence via the undular instability.

3.5. The Undular Instability

The above results demonstrate that the photospheric signatures seen in our simulation exhibit a small-scale, salt-and-pepper structure, arising as a result of field lines dipping in and out of the photosphere. This behavior is largely due to the fact that the emergence process simulated here occurs as a result of the undular instability, also known as the MBI, the theory of which has been studied by numerous authors (Parker 1955; Chandrasekhar 1961; Newcomb 1961; Gough & Tayler 1966; Parker 1966, 1969; Gilman 1970; Tayler 1973; Acheson & Gibbons 1978a, 1978b; Acheson 1979; Spiegel & Weiss 1982; Spruit & van Ballegooijen 1982; Hughes 1985; Hillier 2016, 2018). The MBI mixes plasma above and below the photosphere, and keeps large portions of the magnetic field weighed down with plasma. The instability criterion (Acheson & Gibbons 1978a, 1978b; Acheson 1979; Murray et al. 2006; Archontis et al. 2013) for the undular instability is given by[4]

$$-H_p \frac{1}{|\boldsymbol{B}|}\frac{\partial |\boldsymbol{B}|}{\partial z} > -\frac{1}{2}\beta\gamma\delta + H_p^2 k_\parallel^2\left(1+\frac{k_z^2}{k_\perp^2}\right). \quad (36)$$

[4] Note that other authors (Newcomb 1961; Gilman 1970; Tayler 1973; Fan 2001) give a different form of the instability criterion. However, Acheson & Gibbons (1978b) argue that these alternate forms of the criterion are equivalent. Chandrasekhar (1961) derived a different criterion in the Boussinesq approximation, and Spruit & van Ballegooijen (1982) found a slightly simplified form of the instability criterion using the thin tube approximation. Neither the Boussinesq nor the thin tube approximations are valid in our simulation.

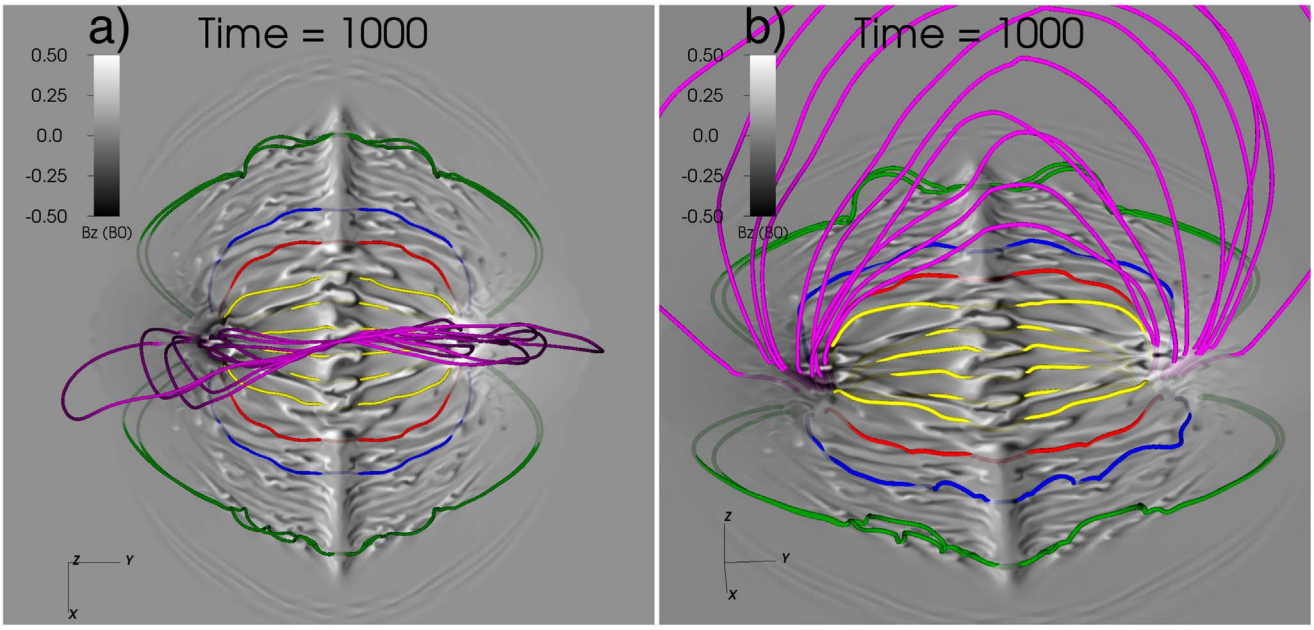

Figure 8. Field lines, overplotted on semitransparent photospheric magnetograms at the end of the simulation, after the emerged lobes haves interacted (see Section 3.6).

Here[5], $H_p = RT_0/g$ is the photospheric pressure scale height, $|\boldsymbol{B}|$ is the magnitude of the magnetic field, β is the ratio of plasma-to-magnetic pressure, $\gamma = 5/3$ is the ratio of specific heats, and

$$\delta = \frac{d\log T}{d\log P} - 1 + \frac{1}{\gamma} \tag{37}$$

is the superadiabatic excess, and is approximately -0.4 in the photosphere. Perturbations have wavevector $\boldsymbol{k}$, where $k_{||}$ and $k_{\perp}$ are the horizontal components parallel and perpendicular to the magnetic field and k_z is the vertical component. Both Murray et al. (2006) and Archontis et al. (2013) found that the second term on the right-hand side is negligible compared to the the first term, so that Equation (36) can be simplified and written (see, e.g., Leake & Linton 2013) as

$$\frac{\xi}{\chi} > 1, \tag{38}$$

where

$$\xi = -\frac{H_p}{|\boldsymbol{B}|}\frac{\partial|\boldsymbol{B}|}{\partial z}, \tag{39}$$

and

$$\chi = -\frac{1}{2}\beta\gamma\delta. \tag{40}$$

Archontis et al. (2013) found that a weakly twisted, initially cylindrical flux rope emerges via the appearance of a pair of lobes of magnetic field when the instability criterion in Equation (38) is satisfied at a height of $\approx$0.3 Mm ($1.76L_0$) above the photosphere. In that simulation, magnetic flux rose from the convection zone and piled up near the photosphere until there was sufficient flux to exceed the instability criterion.

For our simulation, we calculated the criterion in Equation (38) near the time when the peak field strength on the photosphere exceeded $0.05B_0$, as well as at a later time, for reference. In Figure 11, we plot the destabilizing term ξ and the stabilizing term χ at $x = y = 0$ for z near the photosphere around the time when undulations first appear at the photosphere. It is clear that ξ/χ goes from below 1 to above 1 near $t = 800\,t_0$ (black curve), at a height of around $z = z_i = 5L_0$ (0.85 Mm). Here, z_i is defined as the height at which the ratio ξ/χ first reaches unity at $t = 780\,t_0$.

To confirm this, we calculated the total vertical unsigned flux

$$\Phi(z, t) = \int dx\, dy\, |B_z(x, y, z, t)|, \tag{41}$$

at each height at each time step in our simulation, and made a height–time diagram of $\log_{10}(\Phi)$ and $d\log_{10}(\Phi)/dz$, shown in Figure 12. The flux rope is taken to emerge when the peak field strength at the photosphere (shown with the horizontal dashed line) exceeds a relatively modest $0.05B_0$, which occurs at a time marked by the vertical solid line, around $t = 712\,t_0$. It is clear from the figure that a significant amount of flux appears above the photosphere before the instability criterion is exceeded. Furthermore, it appears that the flux rope decelerates as it passes near and through the photosphere, before accelerating upwards again as it expands into the corona, a process known as two-step emergence (Cheung & Isobe 2014). The dashed blue line in the figure tracks the temporal evolution of the height of the maximum value of ξ/χ. Here it is seen that flux builds up above the location of peak ξ/χ, at a height of around $z_i = 5L_0$ above the photosphere—slightly higher than the value found by Archontis et al. (2013)—before rising rapidly around $t = 800$. In addition, in Figure 12 we plot a height–time diagram of the flux of B_y through the $y = 0$ plane as a function

[5] The second term on the right-hand side of Equation (36) is given incorrectly in Archontis et al. (2004) and Archontis et al. (2013). See discussion in Hood et al. (2012).

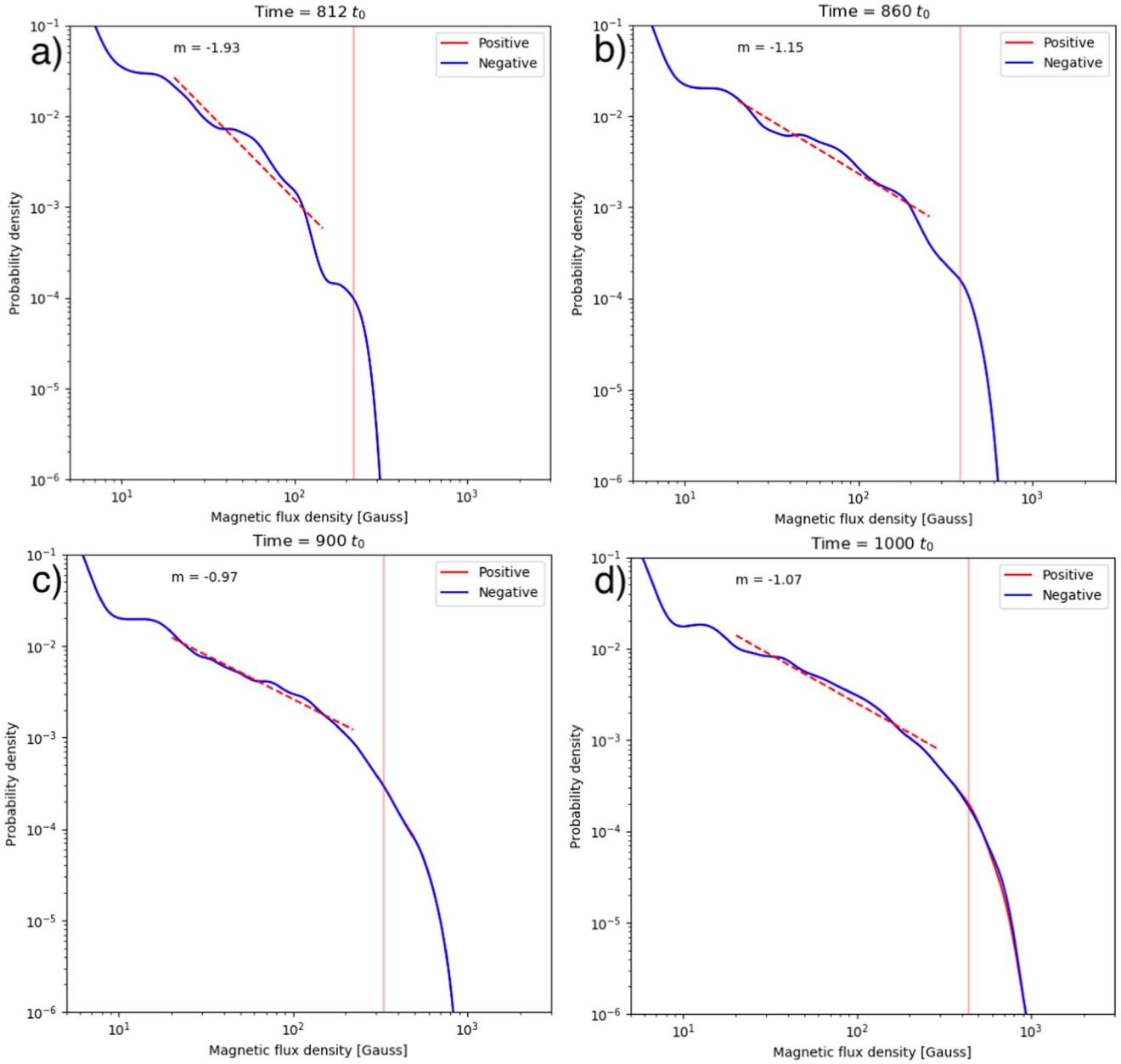

Figure 9. Following Dacie et al. (2017), the probability distribution of magnetic flux at several times during the simulation. The vertical red line shows the value of the magnetic flux density B_{-3}, where the derivative of the probability density curve reached -3, and the slope was fitted between 20 G and $\frac{2}{3}B_{-3}$.

of time:

$$\Phi_h(z, t) = \int_{y=0} dx\delta z(z)\,|B_y(x, z, t)|. \tag{42}$$

This quantity shows the pile-up of flux near the photosphere. Regions of strong B_y pile-up above the photosphere correspond, in panel (b), to locations of large gradients of the vertical flux. Physically, this implies that vertical field lines are bending and turning over just above the photosphere, converting vertical flux into horizontal flux.

This supports the picture of the flux piling up near the photosphere before emerging due to the undular instability. Then, reconnection between adjacent field lines allows the flux to rise rapidly into the corona.

To quantitatively check that this is indeed the undular instability, we measure the wavenumber and growth rate of the instability in our simulation and compare them to theoretical values. Theoretically, the scale of the fastest growing parallel wavenumber of this instability was determined by Acheson & Gibbons (1978a, 1978b), Acheson (1979), Hughes (1985), and Fan (2001), the latter of whom modeled the undular instability in a high-β regime deep in the convection zone as a mechanism to impart buoyancy to flux ropes. These studies found that the fastest growing parallel mode had a wavenumber of order H_p^{-1} (Acheson & Gibbons 1978a, 1978b; Acheson 1979; Hughes 1985) or $0.3\,H_p^{-1}$ (Fan 2001, see their Figure 2).

The scale of the fastest growing perpendicular mode has been studied by numerous authors. Cattaneo et al. (1990) showed that the presence of shear in the field will result in a

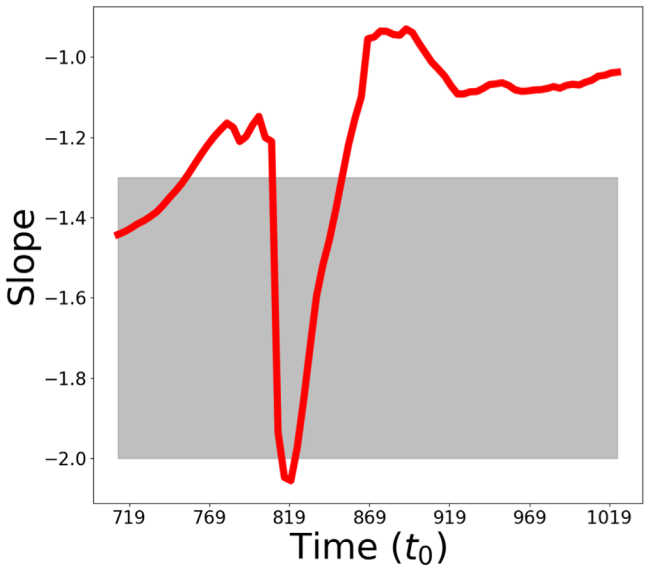

Figure 10. Slope as a function of time for the magnetic field distribution during the simulation. Several snapshots of the distribution are shown in Figure 9. The gray-shaded region is the approximate range of slopes seen in the observational analysis of Dacie et al. (2017, see their Figure 2).

preferred value of $k_\perp$, but we detected little to no shear across the layer, so this is unlikely to set the scale of the perpendicular mode. Fan (2001) argued that a large viscosity could determine the scale of perpendicular modes, since short wavelengths will be damped out. On the other hand, the analysis of Acheson & Gibbons (1978a) and Acheson & Gibbons (1978b) showed that in the presence of small but finite magnetic diffusivity the fastest growing perpendicular mode will also be of order H_p^{-1}, so that the parallel and perpendicular modes should have approximately equivalent wavenumbers. In essence, the fastest growing wavenumbers are those which are large enough to not be damped out by viscous or diffusive effects, but small enough that magnetic tension will not suppress their growth.

To determine the fastest growing wavenumber for our simulation, we took a cut of B_z along the y-direction at $x = 0$ and $z = z_i$ for several times near the initial onset of the instability, around $t = 800\,t_0$ (see Figure 5(b)), corresponding to the parallel direction (i.e., along the flux rope axis). This cut is shown in Figure 13. Although we do not show the distribution of B_z at the height $z = z_i$, it looks extremely similar to the photospheric $z = 0$ distribution, just offset slightly in time. At each time step starting at $t = 800\,t_0$, one of the two central peaks was fit to a sinusoid (green curve) of the form $B_z \sim b_0(t)\sin(k_y y)$. Evidently, the fastest growing parallel wavenumber is of the order

$$k_{||} \approx 0.3\,L_0^{-1}, \tag{43}$$

in agreement with Acheson & Gibbons (1978a, 1978b), Acheson (1979), Hughes (1985), and Fan (2001), and justifying a posteriori our approach of dropping the rightmost term in Equation (36), since this term will be an order of magnitude smaller than either ξ or χ. This wavenumber corresponds to a fastest growing wavelength of

$$\lambda_{||} = \frac{2\pi}{k_{||}} = \frac{2\pi}{0.3} L_0 \approx 21 L_0 \tag{44}$$

(note that $L_0 = H_p$ at the photosphere). This is the wavelength calculated for this instability by many previous authors (Parker 1966, 1969; Shibata et al. 1989; Nozawa et al. 1992). The wavelength of the mode increases slightly in time as the field emerges and the "footpoints" of the field line separate. A similar analysis was performed along the perpendicular (x-) direction at $y = 35$ and $z = z_i$ (the location of this cut is marked by the red line in Figure 5(c), though note that the height of the cut is $z = z_i$, rather than $z = 0$), and fitting to a cosine function as shown in Figure 14. Here the perpendicular mode appears slightly later than the parallel mode, and it is seen to have a wavenumber of order

$$k_\perp \approx 0.55\,L_0^{-1}, \tag{45}$$

corresponding to a perpendicular wavelength of

$$\lambda_\perp = \frac{2\pi}{k_\perp} = \frac{2\pi}{0.55} L_0 \approx 11 L_0. \tag{46}$$

We plot the amplitude of B_z along the two cuts shown in Figures 13 and 14 and stack them in time, as shown in Figure 15. In panel (a), two negative (positive) streaks are clearly visible in the dominant positive (negative) polarity. These are the signatures of the growing parallel mode. Here, it is obvious that the wavelength of the mode is growing in time, since each streak makes an angle with the $y = 0$ axis. In panel (b), the growth of the perpendicular mode can be seen, but in this case the streaks lie almost parallel to the $x = 0$ line, indicating that the wavelength of the perpendicular mode does not change substantially, in agreement with Figure 14.

To determine the growth rate of the instability, in Figure 16 we plot the amplitudes of the modes in Figures 13 and 14 during the very early phase of the evolution. Each five consecutive points along the curve were fit to a running exponential of the form $B_z \sim b_0 e^{\sigma t}$. The color–magnitude diagram shows the value of the growth rate σ along each direction. During the early stages of its growth, the instability has growth rates of order

$$\sigma_{||} \approx 0.15\,t_0^{-1}, \tag{47}$$

and

$$\sigma_\perp \approx 0.20\,t_0^{-1}, \tag{48}$$

in the parallel and perpendicular directions, respectively. In the literature, there are several theoretical estimates for the growth rate of the undular instability. Acheson (1979) estimated the growth rate of the instability to be of order (see Equation (2.7) in Acheson 1979):

$$\sigma \sim \left(\frac{V_a^2}{H_p^2}\xi\right)^{1/2}, \tag{49}$$

with ξ given in Equation (39). At the photosphere, $V_a \approx 1$, and $\xi \approx 0.03$ when the mode amplitude rapidly increases around $t = 800\,t_0$ (see Figure 11) so that (with $H_p = 1$ in our units),

$$\sigma_{\rm Acheson} \approx 0.17\,t_0^{-1}. \tag{50}$$

Thus, the parallel growth rate in our simulation is of the same order of magnitude as the growth rate derived from Acheson (1979).

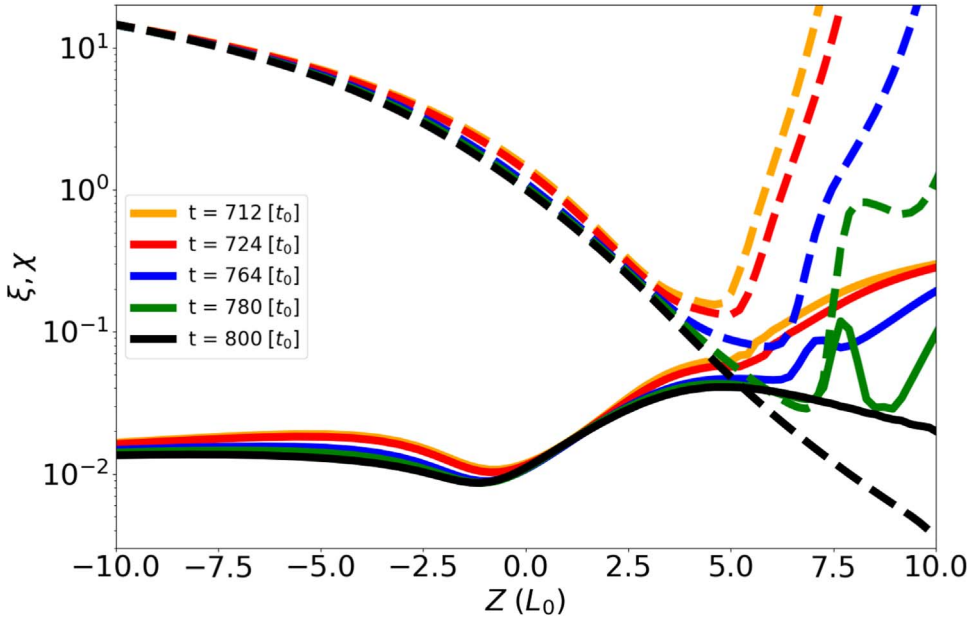

Figure 11. The instability (ξ, solid) and stability (χ, dashed) terms in the magnetic buoyancy relation at several times during the simulation near when the peak photospheric field strength first exceeds $0.05B_0$. The undular mode is unstable when ξ exceeds χ.

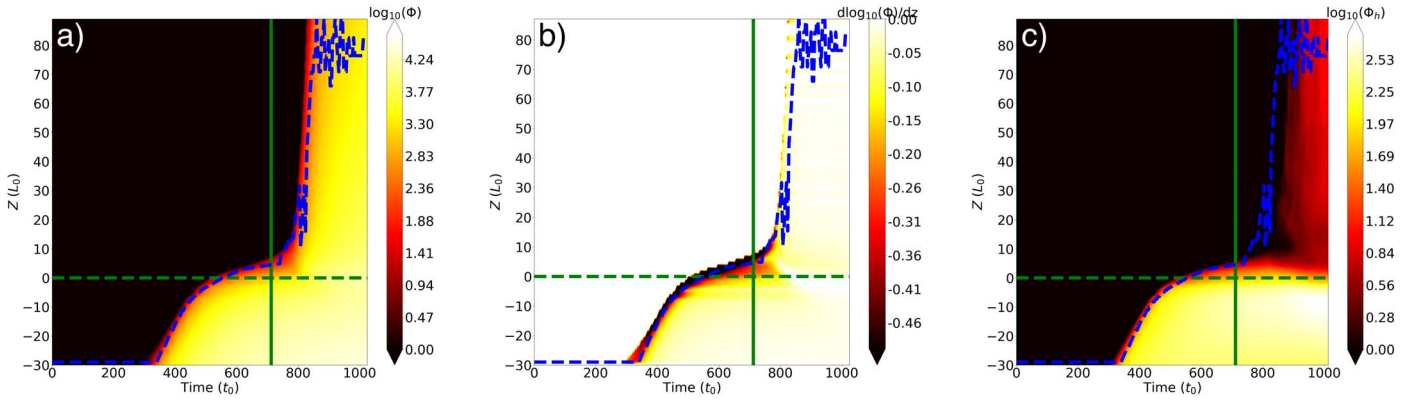

Figure 12. Height–time diagrams of (a) the unsigned vertical magnetic flux, (b) gradient of the unsigned vertical magnetic flux, and (c) the unsigned axial flux through the $y = 0$ plane, showing a fraction of the simulation domain in the z-direction. The horizontal dashed line is at $z = 0$ and the vertical solid line shows the time at which the peak photospheric field strength first exceeds $0.05B_0$. The dashed blue line follows the location of peak ξ/χ as a function of time.

In the high-β regime, Fan (2001), estimated a growth rate for our measured wavenumber of (see Figure 2 in their paper):

$$\sigma_{\rm Fan} \approx 0.1\ t_0^{-1}, \tag{51}$$

which is in good agreement with our measurement during the very initial stages seen in Figure 16.

Chandrasekhar (1961) used the Boussinesq approximation to predict a growth rate of the instability of

$$\sigma = \left[\frac{g\sqrt{k_\perp^2 + k_{||}^2}}{(\rho_+ + \rho_-)} \delta\rho_{\rm ph} - \frac{(k_{||} B_y)^2}{2\pi(\rho_+ + \rho_-)} \right]^{1/2}, \tag{52}$$

where g is gravity, $k_{||} = k_y$ and $k_\perp = k_x$ are the wavenumbers parallel and perpendicular to the magnetic field $\boldsymbol{B}$, and ρ_+ and ρ_- are the densities above and below the unstable layer, with density difference $\delta\rho_{\rm ph}$. Although in our simulation, $\delta\rho_{\rm ph}/\rho_{\rm ph} \sim O(1)$ at the photosphere, and the Boussinesq approximation is not applicable, we can, nevertheless, test how close the growth rate derived from this approximation is to the one measured here. Averaging ρ_+, ρ_-, and B_y^2 over the interface region $x, y \in [-50, 50]\ L_0$ yields

$$\sigma_{\rm Chandrasekhar} \approx 0.31\ t_0^{-1}, \tag{53}$$

which is in good agreement with the growth rate shown in Figure 16. Evidently, the growth rate for this instability derived in the Boussinesq regime, which is admittedly inapplicable in our simulation, produces values that are in good agreement with our simulation results.

Thus, both the fastest growing parallel and perpendicular wavenumbers and growth rates of the instability observed in our simulation are in reasonable agreement with theoretical predictions of these same quantities in the undular instability.

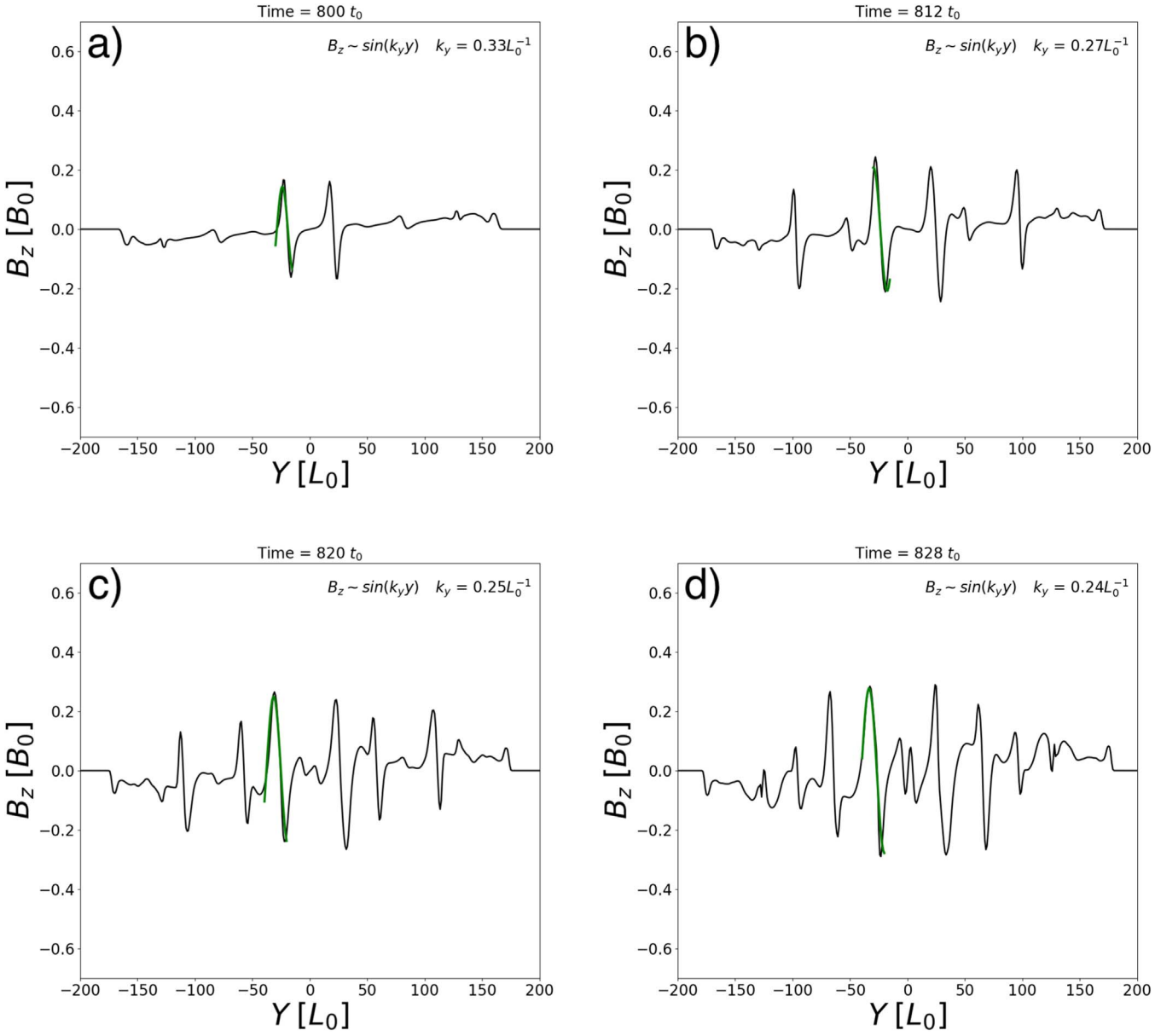

Figure 13. A line cut of B_z at $z = z_i$ along the y-direction at $x = 0$ at several different times during the linear stage of the instability. The green line marks a segment of the curve that was fit to a sinusoid with wavenumber k_y, and its amplitude is analyzed in Figure 16. For reference, the legs of the emerging flux center at $\pm y = 120\,L_0$.

3.6. Interaction of the Lobes

The emergence of magnetic lobes was found by Archontis et al. (2013) to result in significant reconnection and a jet-like disturbance in the corona. In our simulation, we see a similar event around $t = 820\,t_0$ that may affect the linear evolution of the undular mode, which stops around the same time. Figure 17 shows the magnetic energy

$$W_m = \frac{1}{2\mu_0}\int_{z>0} dV\ B^2, \tag{54}$$

and kinetic energy

$$W_k = \frac{1}{2}\int_{z>0} dV\ \rho v^2 \tag{55}$$

in the corona as a function of time. The decrease in the magnetic energy that starts around $t = 824\,t_0$ (green line) corresponds approximately to the same magnitude increase in the kinetic energy which peaks at $t = 864\,t_0$ (blue line). In Figure 18, we plot a series of field lines, seeded along a vertical line at ($x = y = 0$, $z > 0$) in the corona on top of vertical cuts of the vertical velocity V_z. The field lines are colored by B_z. Early in the interaction, at $t = 824\,t_0$, the field lines only barely extend above the photosphere. They slowly rise, and it is clear that by $t = 860\,t_0$, the two primary lobes are interacting, and field lines with opposite signs of B_z begin to reconnect. This creates a significant upflow, as the newly reconnected concave up field lines release their tension. This upflow is only seen low down in the corona before $t = 860\,t_0$, and with much smaller magnitude, since the field is not significantly expanding into the corona, but by $t = 880\,t_0$ and $t = 900\,t_0$ there is a clear upflow visible in the corona along with a concave-down arcade overlying the interacting loops. This type of event likely

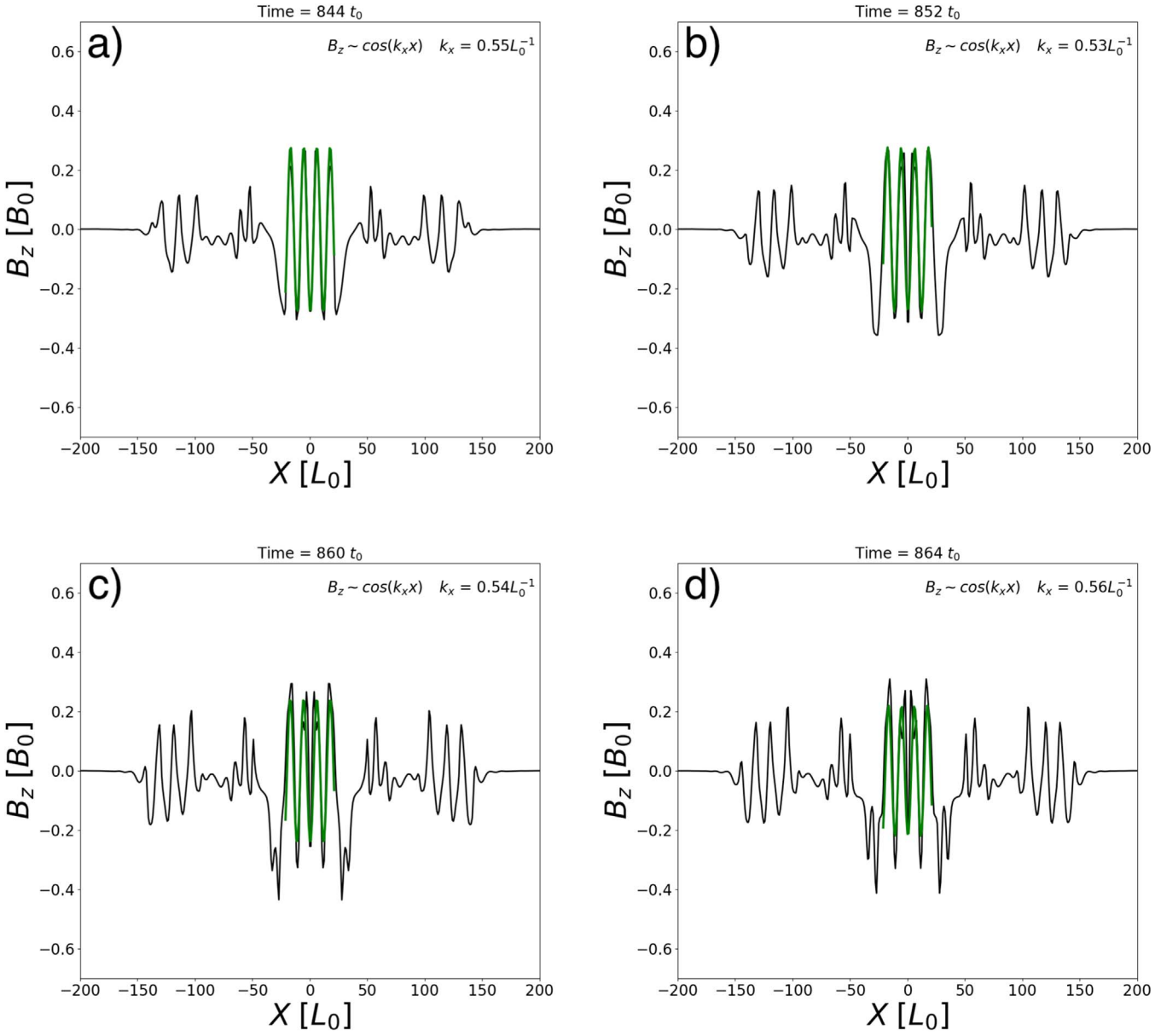

Figure 14. A line cut of B_z at $z = z_i$ along the x-direction at $y = 35$ at several different times during the linear stage of the instability. The green line marks a segment of the curve that was fit to a cosinusoid with wavenumber k_x, and its amplitude is analyzed in Figure 16.

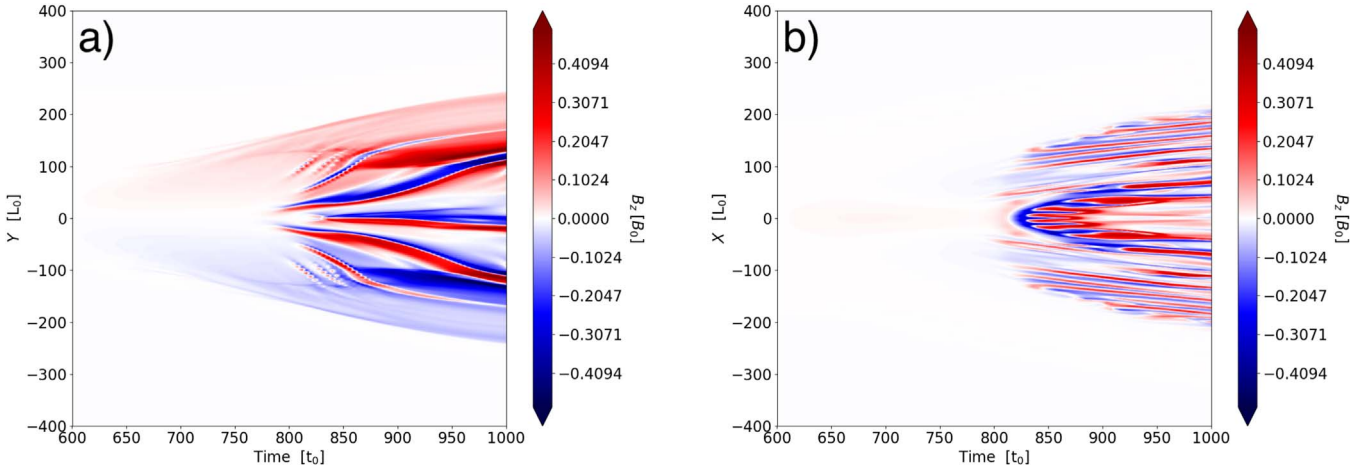

Figure 15. Distance–time plot of B_z along the (a) y- and (b) x-directions.

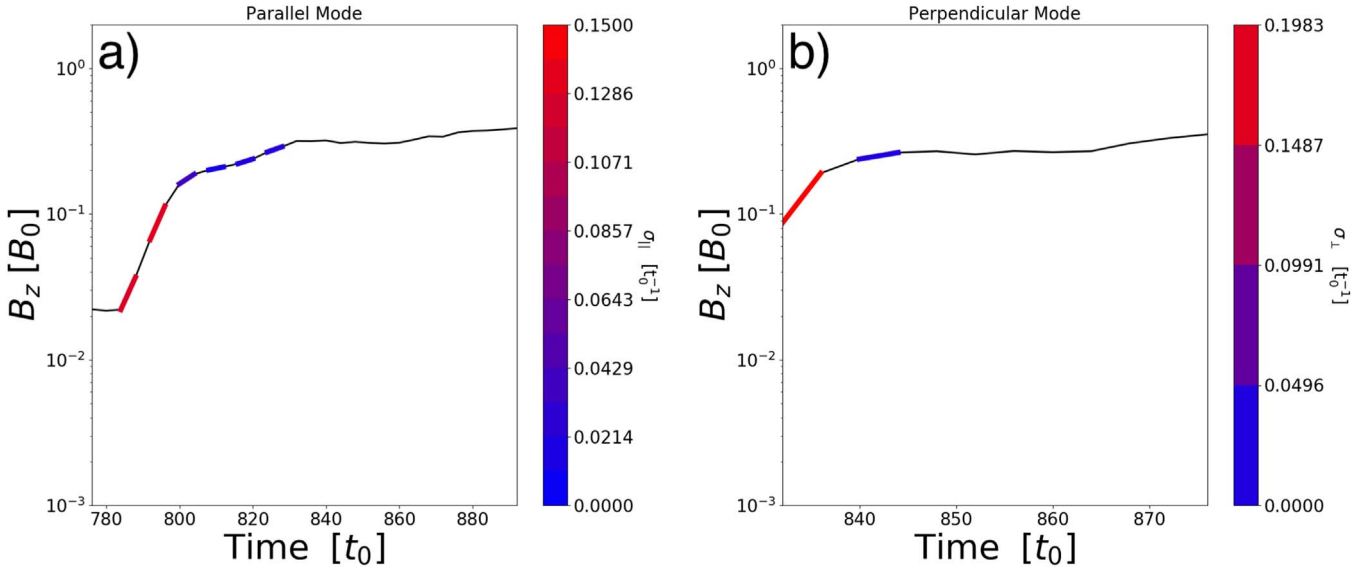

Figure 16. Amplitudes of the modes shown in Figures 13 and 14, representing the growth of the parallel (a) and perpendicular (b) modes. Each five consecutive points along the curve were fit to an exponential of the form $B_z \sim b_0 e^{\sigma t}$, and the color shading represents the value of σ in the parallel (a) and perpendicular (b) directions.

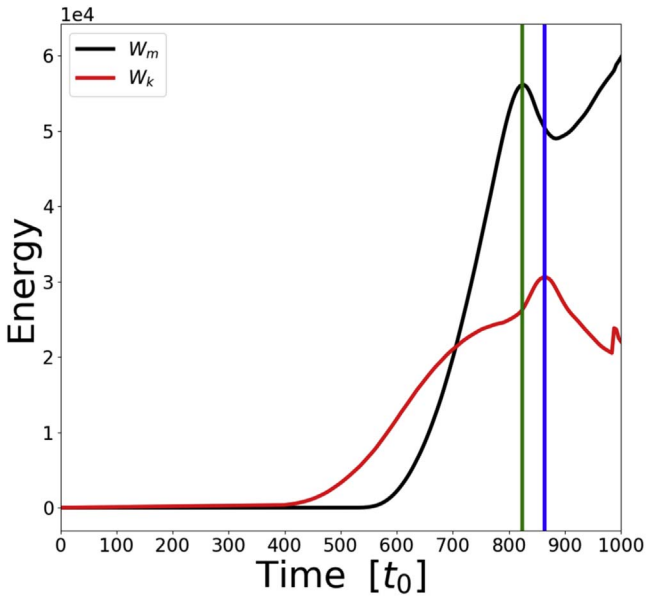

Figure 17. Magnetic energy (black) and kinetic energy (red) in the corona as a function of time. The green (blue) line at $t = 824\ t_0$ ($t = 864\ t_0$) shows the local maximum of the magnetic (kinetic) energy.

represents an Ellerman bomb, which is associated with this type of topology (Pariat et al. 2004, 2006, 2009; Isobe et al. 2007; Archontis & Hood 2009; Danilovic 2017).

4. Conclusions

In this paper, we simulated the buoyant rise and emergence of an untwisted toroidal flux rope from deep in the convection zone. The flux rope is able to rise coherently through the convection zone, emerge through the photosphere, and form a relatively large (≈40 Mm across) active region. The emergence mechanism of our flux rope is identified to be the undular instability (Parker 1977; Acheson 1979; Fan 2001; Archontis et al. 2013). The instability is responsible for creating an active region displaying lots of salt-and-pepper flux concentrations, which have previously been identified as the result of convective flows destroying the rising flux rope (Rempel & Cheung 2014; Dacie et al. 2017). However, the simulation presented here shows that the undular instability is a second mechanism that could account for the presence of salt-and-pepper structures on the photosphere. The structures formed in this simulation resemble those seen in observations (Kitiashvili et al. 2015; Dacie et al. 2017). Toriumi & Yokoyama (2012) found similar salt-and-pepper structures, however, their structures are due to a fluting instability, which produces more wavelengths and more regular structures than are seen here.

Our work demonstrates that, contrary to many previous works, there is no minimum twist required for the flux rope to be able to rise and emerge from the convection zone into the corona (Parker 1979; Schuessler 1979; Longcope et al. 1996; Moreno-Insertis & Emonet 1996; Emonet & Moreno-Insertis 1998; Fan et al. 1998; Wissink et al. 2000; Murray et al. 2006; Toriumi & Yokoyama 2011). Our results raise the question of why the untwisted flux rope presented here was able to both rise and emerge coherently, while many other twisted flux ropes, for example, the weakly twisted flux ropes of Murray et al. (2006) and Toriumi & Yokoyama (2011) were not able to rise and emerge. One possible answer for why this flux rope was able to rise coherently is that the toroidal shape of our flux rope plays an important role. Abbett et al. (2000) argued that in three dimensions, the viscous forces that destroy the flux rope do so only over a segment of the flux rope, and that if this segment is sufficiently short (for example, if the flux rope were sufficiently curved, as in a torus), then an untwisted flux rope would not be fragmented and could rise coherently. To test this hypothesis, we performed a 2.5D simulation of an untwisted cylindrical flux rope cross section with the same simulation parameters as described above, except that the tube is a cylinder rather than a torus, and the variables along the ignorable direction (y, corresponding to the axial direction of the cylinder) were considered translationally invariant. Contours of $|B|$ are shown in Figure 19. Evidently, this flux rope rises a short distance and then breaks up into separate segments on either side of $x = 0$, and when it reaches the photosphere it spreads out, rather than emerging. Comparing Figures 4 and

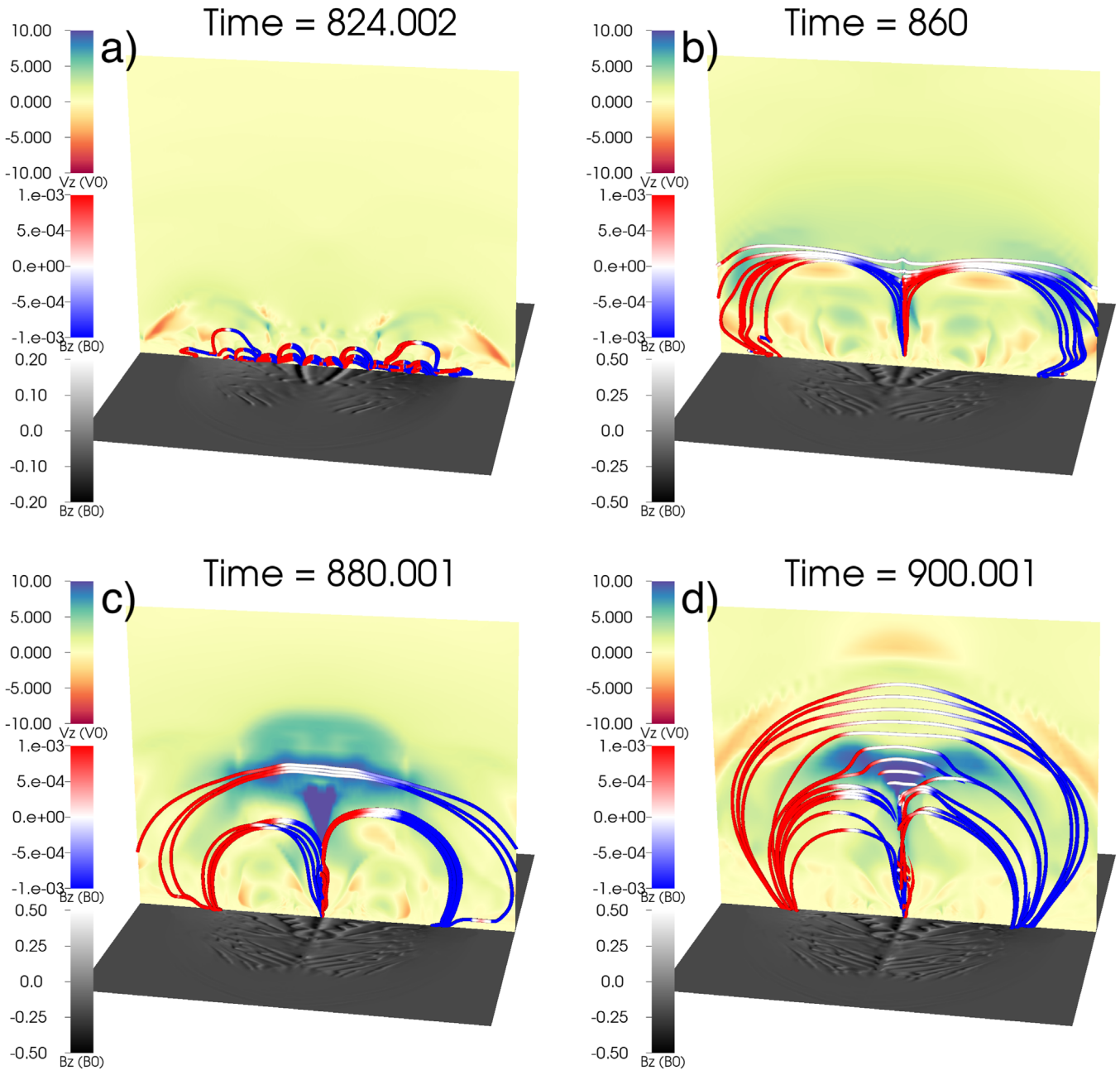

Figure 18. Field lines colored by B_z overplotted on a vertical plane of V_z and a photospheric magnetogram at several times before and during the reconnection event.

19, it is clear that these are two fundamentally different behaviors, and clearly the curved three-dimensional structure of the toroidal flux rope plays an important role in the coherent rise of that flux rope, either because viscous forces on a torus are important only over a very short segment, or because plasma is able effectively to drain down the legs of the rising torus. This lends credence to the hypothesis that the toroidal shape of the flux rope is crucial to a coherent rise and emergence. Finally, the coherence of the rising torus may also be facilitated by the line-tied boundary conditions, which prevent flux from diffusing or spreading out near the bottom of the torus.

The emergence process that we observed is in line with the findings of other studies that simulated the rise of weakly twisted flux ropes. Archontis et al. (2013) demonstrated that a weakly twisted flux rope, rather than forming a single concave-down overarching quasi-potential loop in the corona, formed instead two concave-down loops in the corona, which then reconnected. At the photosphere, they showed that, rather than forming a pair of opposite polarity regions—as is typical for moderately twisted flux ropes—the flux rope formed two extended opposite polarities between the two primary polarities. Our toroidal simulations corroborate this result, with the additional finding that there is a significant amount of salt-and-pepper structure dispersed throughout the active region. In other words, there are many magnetic field undulations, as opposed to just the two seen in Archontis et al. (2013).

A key question from this study is why do some flux ropes emerge in convectively stable simulations with the salt-and-pepper structure indicative of the undular instability (Archontis et al. 2013, this work), whereas other flux ropes emerge with little to no evidence of such structure (e.g.,

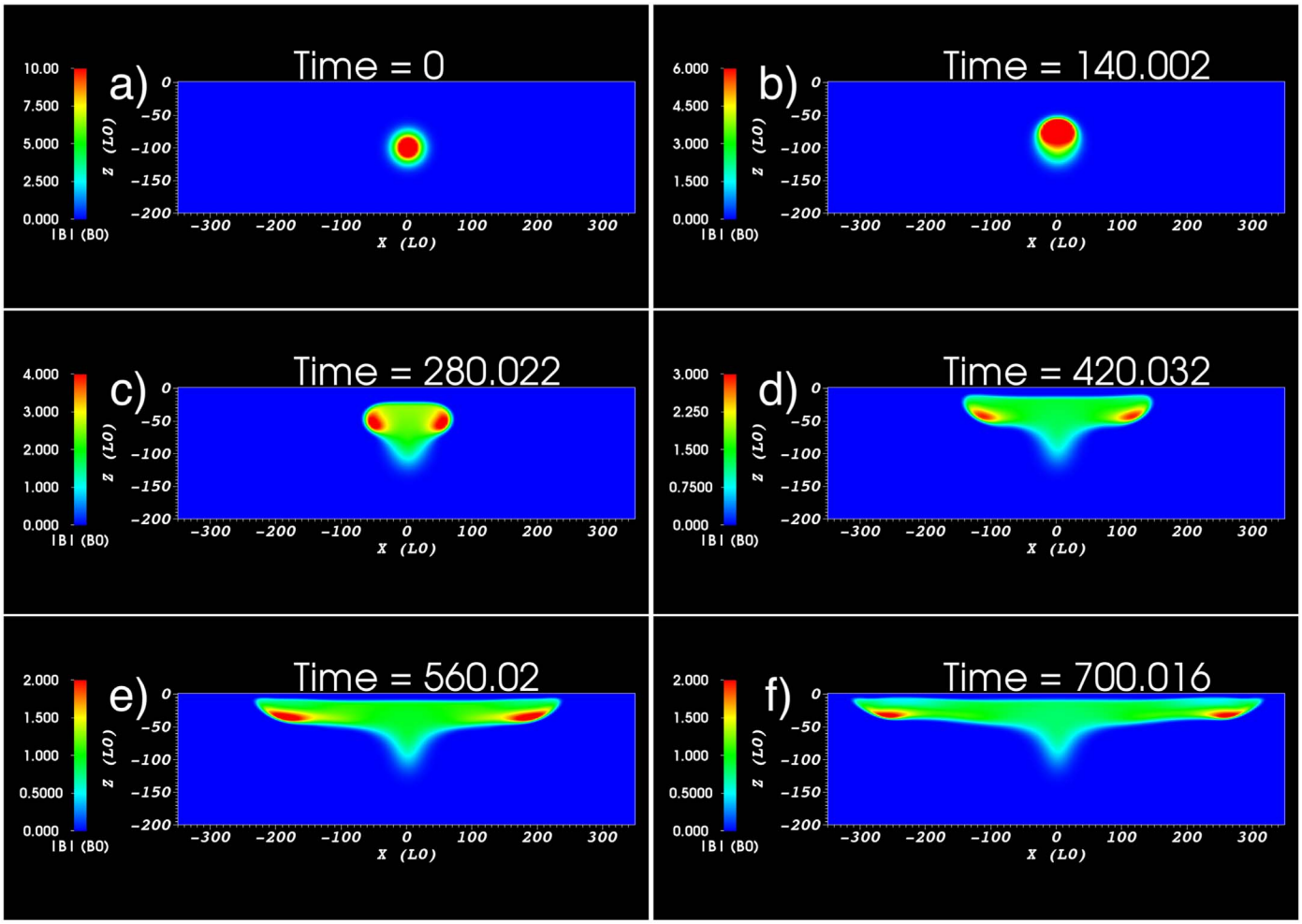

Figure 19. Contours of $|B|$ at different times during the 2.5D simulation in the x–z plane.

MacTaggart & Hood 2009; Toriumi & Yokoyama 2011; Leake et al. 2013; Toriumi & Takasao 2017; Knizhnik et al. 2018)? We suggest that there are several factors that influence the presence of salt-and-pepper features at the photospheric level. One required property of flux emergence simulations to see these features is that the width of the active region should be at least several wavelengths of the undular mode. The fastest growing wavenumber of $\approx 0.3\, L_0^{-1}$, corresponds to a wavelength of $\approx 21\, L_0$, so that the resulting active region needs to be several times this size. The simulations of Knizhnik et al. (2018), for example, had a width of only about $50\, L_0$, so that only about two wavelengths could have been seen. At this scale, salt-and-pepper features would be difficult to identify. Similarly, the simulations of Leake et al. (2013) and MacTaggart & Hood (2009) formed an active region of approximate width $60\, L_0$, so they would be expected to have only seen about three wavelengths, not enough to see a large number of salt-and-pepper features.

This cannot be the complete answer, however, since (1) two or three wavelengths of the undular mode should still have been noticed, and (2) the simulation of Archontis et al. (2013) was approximately the same size as that of Knizhnik et al. (2018), and yet the former observed the presence of undular field lines, while the latter did not. Conversely, some simulations with large active regions, such as the simulation of Toriumi & Takasao (2017), with an active region of width $\approx 100\, L_0$, show no sign of undulating field lines. One difference between the studies of Archontis et al. (2013) and Knizhnik et al. (2018) is that the flux rope of Archontis et al. (2013) was twisted only weakly. It is possible that this prevented emergence for long enough that a significant gradient in the magnetic field was able to build up, triggering the onset of the instability. On the other hand, the simulation of Toriumi & Takasao (2017) with no undular signatures had a smaller twist than that used by Archontis et al. (2013), so this cannot be the complete picture either. More investigation is needed into why some flux emergence simulations produce salt-and-pepper structure resulting from undulating field lines, while other simulations do not.

Another important factor to consider in determining whether emergence occurs is the time required for a significant amplitude of the instability to set in. Since the instability criterion in Equation (36) depends on β and the vertical magnetic field gradient, it is clear that strong gradients in the magnetic field and small values of β (corresponding to strong magnetic fields) are crucial to the emergence of flux ropes through the photosphere. In the case of Murray et al. (2006) and Toriumi & Yokoyama (2011), it is possible that the simulation was not run long enough to allow for a sufficient amount of magnetic field to pile-up below the photosphere to generate a strong vertical gradient in $\boldsymbol{B}$, or to lower the β sufficiently. This evidence is supported by the results of

Archontis et al. (2013), who were able to obtain an emerged flux rope by extending the duration of the simulation. For a growth rate of order $0.2\,t_0^{-1}$ (see Figure 16), a significant amplitude of the instability can be obtained within a time period of order 20–50 t_0. While this may explain the lack of emergence in Murray et al. (2006), Toriumi & Yokoyama (2011) allowed the simulation to run for several hundred t_0 after the flux rope neared the photosphere, so more work is required to understand why their flux rope did not emerge. The magnitude of the vertical gradient is influenced by the scale of the original flux rope as well as its initial field strength, and in turn, how both of these quantities change when the flux rope reaches the photosphere. It is possible that one or both of these quantities were not sufficiently large for the instability criterion to be exceeded.

To summarize, we hypothesize that there are several key factors needed in order for a convection free simulation to produce the salt-and-pepper structure seen here: (1) continual piling up of magnetic flux near the photosphere, enabling the upward magnetic pressure gradient to grow until it is large enough to lift the heavy photospheric plasma. This is a general criterion for flux emergence, and without a strong magnetic gradient no flux will appear at the photosphere. (2) The flux rope must be untwisted or twisted only weakly. Strong twist allows the flux rope to maintain its circular cross section, and the downward concavity of the rising field lines will facilitate emergence through the photosphere. On the other hand, a weak twist allows the flux rope to expand and become more horizontal. (3) The active region produced by the emerged flux rope must be sufficiently large in order to observe multiple wavelengths of the undular instability.

Finally, the role of convection in flux emergence is also important to understand. Previous studies have argued that weakly twisted flux ropes, in particular, require convective upflows to emerge, since these counteract the deceleration of the flux ropes caused by their fragmentation (Abbett 2007; Cheung et al. 2007; Isobe et al. 2008; Dacie et al. 2017). However, our results demonstrate that convection is not necessary for the emergence of weakly twisted flux ropes. On the other hand, convection could also act to break up a weakly twisted flux rope and produce more small-scale flux, or, instead, could act to concentrate flux bundles together, which would bring the kernel density estimations at large field strengths, shown in Figure 9, more in line with observations. Many previous global-scale convective flux emergence simulations employ the anelastic approximation, which becomes invalid 20–30 Mm below the photosphere. As shown above, this is an important region where flux piles up, and thus parameter surveys of twist (e.g., Fan 2008; Jouve et al. 2013) cannot answer definitively whether weakly twisted flux ropes will emerge. Further work is required to determine the role that convection plays in flux emergence.

K.J.K. was supported for this work by the Office of Naval Research through the National Research Council, the Jerome and Isabella Karle Distinguished Scholar Fellowship and NASA's Heliophysics Supporting Research Program. J.E.L. was supported by NASA LWS and ISFM programs. M.G.L. was supported for this work by the Office of Naval Research 6.1 program and by the NASA Living with a Star Program and Heliophysics Supporting Research programs. K.J.K. would like to acknowledge helpful discussions with A. Hillier. The numerical simulations were performed under the grant of computer time at the Department of Defense High Performance Computing Program. The authors are grateful to the anonymous referee who greatly improved the quality and scope of this work.

ORCID iDs

K. J. Knizhnik https://orcid.org/0000-0002-2544-2927
J. E. Leake https://orcid.org/0000-0002-6936-9995
S. Dacie https://orcid.org/0000-0001-7572-2903

References

Abbett, W. P. 2007, ApJ, 665, 1469
Abbett, W. P., Fisher, G. H., & Fan, Y. 2000, ApJ, 540, 548
Acheson, D. J. 1979, SoPh, 62, 23
Acheson, D. J., & Gibbons, M. P. 1978a, JFM, 85, 743
Acheson, D. J., & Gibbons, M. P. 1978b, RSPTA, 289, 459
Arber, T. D., Longbottom, A. W., Gerrard, C. L., & Milne, A. M. 2001, JCoPh, 171, 151
Archontis, V., & Hood, A. W. 2009, A&A, 508, 1469
Archontis, V., Hood, A. W., & Tsinganos, K. 2013, ApJ, 778, 42
Archontis, V., Moreno-Insertis, F., Galsgaard, K., Hood, A., & O'Shea, E. 2004, A&A, 426, 1047
Batchelor, G. K. 2000, An Introduction to Fluid Dynamics (Cambridge: Cambridge Univ. Press)
Cattaneo, F., Chiueh, T., & Hughes, D. W. 1990, JFM, 219, 1
Chandrasekhar, S. 1961, Hydrodynamic and Hydromagnetic Stability (Oxford: Clarendon)
Cheung, M. C. M., & Isobe, H. 2014, LRSP, 11, 3
Cheung, M. C. M., Schüssler, M., & Moreno-Insertis, F. 2007, A&A, 467, 703
Dacie, S., Démoulin, P., van Driel-Gesztelyi, L., et al. 2016, A&A, 596, A69
Dacie, S., van Driel-Gesztelyi, L., Démoulin, P., et al. 2017, A&A, 606, A34
Danilovic, S. 2017, A&A, 601, A122
D'Silva, S., & Choudhuri, A. R. 1993, A&A, 272, 621
Emonet, T., & Moreno-Insertis, F. 1998, ApJ, 492, 804
Fan, Y. 2001, ApJ, 546, 509
Fan, Y. 2008, ApJ, 676, 680
Fan, Y. 2009, ApJ, 697, 1529
Fan, Y., Fisher, G. H., & Deluca, E. E. 1993, ApJ, 405, 390
Fan, Y., Zweibel, E. G., & Lantz, S. R. 1998, ApJ, 493, 480
Galsgaard, K., Archontis, V., Moreno-Insertis, F., & Hood, A. W. 2007, ApJ, 666, 516
Gilman, P. A. 1970, ApJ, 162, 1019
Gough, D. O., & Tayler, R. J. 1966, MNRAS, 133, 85
Hillier, A. 2018, RvMPP, 2, 1
Hillier, A. S. 2016, MNRAS, 462, 2256
Hood, A. W., Archontis, V., & MacTaggart, D. 2012, SoPh, 278, 3
Hughes, D. W. 1985, GApFD, 32, 273
Isobe, H., Proctor, M. R. E., & Weiss, N. O. 2008, ApJL, 679, L57
Isobe, H., Tripathi, D., & Archontis, V. 2007, ApJL, 657, L53
Jouve, L., Brun, A. S., & Aulanier, G. 2013, ApJ, 762, 4
Kitiashvili, I. N., Kosovichev, A. G., Mansour, N. N., & Wray, A. A. 2015, ApJ, 809, 84
Knizhnik, K. J., Linton, M. G., & DeVore, C. R. 2018, ApJ, 864, 89
Landau, L. D., & Lifshitz, E. M. 1987, Fluid Mechanics (2nd ed.; Oxford: Pergamon)
Leake, J. E., & Linton, M. G. 2013, ApJ, 764, 54
Leake, J. E., Linton, M. G., & Török, T. 2013, ApJ, 778, 99
Longcope, D., Linton, M., Pevtsov, A., Fisher, G., & Klapper, I. 1999, GMS, 111, 93
Longcope, D. W., Fisher, G. H., & Arendt, S. 1996, ApJ, 464, 999
Longcope, D. W., Fisher, G. H., & Pevtsov, A. A. 1998, ApJ, 507, 417
MacTaggart, D., & Hood, A. W. 2009, A&A, 507, 995
Moffatt, H. K. 1978, Magnetic Field Generation in Electrically Conducting Fluids (Cambridge: Cambridge Univ. Press)
Moreno-Insertis, F., Caligari, P., & Schuessler, M. 1994, SoPh, 153, 449
Moreno-Insertis, F., & Emonet, T. 1996, ApJL, 472, L53
Murray, M. J., Hood, A. W., Moreno-Insertis, F., Galsgaard, K., & Archontis, V. 2006, A&A, 460, 909
Nelson, N. J., & Miesch, M. S. 2014, PPCF, 56, 064004
Newcomb, W. A. 1961, PhFl, 4, 391
Nozawa, S., Shibata, K., Matsumoto, R., et al. 1992, ApJS, 78, 267

Pariat, E., Aulanier, G., Schmieder, B., et al. 2004, ApJ, 614, 1099
Pariat, E., Aulanier, G., Schmieder, B., et al. 2006, AdSpR, 38, 902
Pariat, E., Masson, S., & Aulanier, G. 2009, ApJ, 701, 1911
Parker, E. N. 1955, ApJ, 121, 491
Parker, E. N. 1966, ApJ, 145, 811
Parker, E. N. 1969, SSRv, 9, 651
Parker, E. N. 1977, ApJ, 215, 370
Parker, E. N. 1979, Cosmical Magnetic Fields. Their Origin and their Activity (Oxford: Clarendon)
Pevtsov, A. A., Canfield, R. C., & McClymont, A. e. N. 1997, ApJ, 481, 973
Pevtsov, A. A., Canfield, R. C., & Metcalf, T. R. 1994, ApJL, 425, L117
Pevtsov, A. A., Canfield, R. C., & Metcalf, T. R. 1995, ApJL, 440, L109
Rempel, M., & Cheung, M. C. M. 2014, ApJ, 785, 90
Schuessler, M. 1979, A&A, 71, 79
Schussler, M., Caligari, P., Ferriz-Mas, A., & Moreno-Insertis, F. 1994, A&A, 281, L69
Shibata, K., Tajima, T., Steinolfson, R. S., & Matsumoto, R. 1989, ApJ, 345, 584
Spiegel, E. A., & Weiss, N. O. 1982, GApFD, 22, 219
Spruit, H. C., & van Ballegooijen, A. A. 1982, A&A, 106, 58
Tayler, R. J. 1973, MNRAS, 161, 365
Thomas, J. H., & Nye, A. H. 1975, PhFl, 18, 490
Toriumi, S., & Takasao, S. 2017, ApJ, 850, 39
Toriumi, S., & Yokoyama, T. 2010, ApJ, 714, 505
Toriumi, S., & Yokoyama, T. 2011, ApJ, 735, 126
Toriumi, S., & Yokoyama, T. 2012, A&A, 539, A22
Wissink, J. G., Matthews, P. C., Hughes, D. W., & Proctor, M. R. E. 2000, ApJ, 536, 982